Astronomical Pacing of Middle Eocene Sea-Level Fluctuations: Inferences From Shallow-Water Carbonate Ramp Deposits

T C Brachert, C Agnini, C Gagnaison, Jean-Pierre Gély, M J Henehan, T Westerhold

Paleoceanography and Paleoclimatology

RESEARCH ARTICLE
10.1029/2023PA004633

Special Section:
Illuminating a Warmer World: Insights from the Paleogene

Astronomical Pacing of Middle Eocene Sea-Level Fluctuations: Inferences From Shallow-Water Carbonate Ramp Deposits

T. C. Brachert[1], C. Agnini[2], C. Gagnaison[3], J.-P. Gély[4], M. J. Henehan[5,6], and T. Westerhold[7]

[1]Institute for Earth System Science and Remote Sensing, Leipzig, Germany, [2]Dipartimento di Geoscienze, Universita degli Studi di Padova, Padova, Italy, [3]Departement de Geosciences, B2R-EA 7511, UniLaSalle, Beauvais, France, [4]Université Paris 1, Panthéon-Sorbonne, LAMOP, UMR 8589, CNRS, Paris, France, [5]GFZ German Research Centre for Geosciences, Potsdam, Germany, [6]School of Earth Sciences, University of Bristol, Bristol, UK, [7]MARUM—Center for Marine Environmental Sciences, University of Bremen, Bremen, Germany

Abstract Astrochronologically calibrated deep-sea records document the Cenozoic (66–0 Ma) global climatic cooling in great detail, but the magnitude of sea-level fluctuations of the middle Eocene Warmhouse state (47.8–37.7 Ma) and the ~40.3 Ma warming event of the Middle Eocene Climatic Optimum (MECO) is not well constrained. Here, we present a sequence stratigraphic classification of a shallow marine mixed carbonate—clastic ramp system for this time interval in Paris basin, France. Based on sedimentologic, paleogeographic and biostratigraphic data, we hypothesize that the 22 elementary sequences recognized each correspond to the long cycle of orbital eccentricity (0.405 Myr). With the exception of the MECO, the shoreline trajectory of superimposed, third-order depositional sequences evolved in phase with the very long cycles of orbital eccentricity (2.4 Myr), suggesting significant polar ice build-up leading to sea level lowstands during nodes of the very long eccentricity cycle. Inferred from Fischer Plot methodology, Lutetian third-order eustasy was in the order of 5–10 m and during the MECO 30 m or more. Furthermore, the shallow-water record implies that third order sea-level changes were astronomically paced in the middle Eocene Warmhouse climate state, but a decoupling occurred during the transient MECO warming.

Key Points:

- Astronomical calibration of shallow water carbonates
- Eocene sea-level changes paced by very long eccentricity
- Insolation driven sea-level changes (third order) were 5–10 m

Supporting Information:

Supporting Information may be found in the online version of this article.

Correspondence to:

T. C. Brachert,
brachert@uni-leipzig.de

Citation:

Brachert, T. C., Agnini, C., Gagnaison, C., Gély, J.-P., Henehan, M. J., & Westerhold, T. (2023). Astronomical pacing of middle Eocene sea-level fluctuations: Inferences from shallow-water carbonate ramp deposits. *Paleoceanography and Paleoclimatology*, *38*, e2023PA004633. https://doi.org/10.1029/2023PA004633

Received 1 MAR 2023
Accepted 19 OCT 2023

Author Contributions:

Conceptualization: T. C. Brachert, T. Westerhold
Funding acquisition: T. C. Brachert
Methodology: T. C. Brachert, C. Agnini, C. Gagnaison, J.-P. Gély, M. J. Henehan, T. Westerhold
Project Administration: T. C. Brachert
Supervision: T. C. Brachert
Visualization: T. C. Brachert
Writing – original draft: T. C. Brachert

1. Introduction

Over geological history, global mean sea level underwent substantial fluctuations (Haq et al., 1987; Hardenbol et al., 1998; Miller et al., 2020). These fluctuations resulted from crustal depth changes of the oceanic basins and/or variations of seawater volume by thermal and cryospheric dynamics (glacioeustasy) (Miller et al., 2005). Thermal and glacioeustatic sea-level fluctuations are best identified using combined proxies of bottom water temperature and cryospheric dynamics in deep-sea sediments, such as the $\delta^{18}O$ value of benthic foraminifers (Miller et al., 2020). Benthic foraminifer $\delta^{18}O$ data track the ice sheet evolution on the continents and mean deep-sea temperature, the latter set by surface conditions at sites of water mass formation. Disentangling ice and temperature effects in the $\delta^{18}O$ signatures requires a combination of $\delta^{18}O$ data with information from other temperature-dependent proxies, for example, the Mg concentration in calcite tests of benthic foraminifers (Mg/Ca ratios) (Miller et al., 2020). For some time periods of the early Cenozoic and especially for the short-term (transient) warming events of the Paleogene (hyperthermals), deep-sea Mg/Ca temperatures are little constrained and the occurrence and magnitude of possible thermal and/or glacioeustatic sea-level fluctuations are disputed (Miller et al., 2020). In this respect, combined $\delta^{18}O$-Mg/Ca temperature reconstructions for the Paleocene and early Eocene could yield questionable temperatures, unrealistic sea-level reconstructions, or both (Cramer et al., 2011; Miller et al., 2020).

Compared to the Paleocene/Eocene Thermal Maximum and early Eocene hyperthermal events, the transient warming of the Middle Eocene Climatic Optimum (MECO) ~40 million years (Ma) ago is peculiar. It differs by its comparatively long duration of ~0.4 Ma and the absence of an ubiquitous negative carbon isotope excursion (e.g., Bohaty et al., 2009; Henehan et al., 2020). It has been suggested, that MECO warming was due to atmospheric CO_2 increases by paroxysmal continental arc volcanism (Sluijs et al., 2013; van der Boon et al., 2021). While some proxy studies link the negative oxygen isotope excursion (OIE) ~1‰ of the MECO to a global temperature increase of 3–6°C (Bohaty et al., 2009; Bohaty & Zachos, 2003; Cramwinckel et al., 2018), the extent of a possible parallel sea-level rise that may have reached ~65 m is controversial (e.g., Edgar et al., 2007; Miller et al., 2020; Tripati et al., 2005). In contrast, carbon cycle modeling does find a small shift in shelf:open

Writing – review & editing: T. C. Brachert, C. Agnini, C. Gagnaison, J.-P. Gély, M. J. Henehan, T. Westerhold

ocean carbonate production ratio—such as would be expected from moderate sea level rise—helps to reconcile patterns of deep sea carbonate preservation (Sluijs et al., 2013). Proxy data from deep-sea cores and onshore outcrops of deep-sea sediments using astrochronologically calibrated age models now provide a reasonably coherent picture of the MECO, although problems related to inconsistent age models remain (Giorgioni et al., 2019; Rivero-Cuesta et al., 2019; Westerhold et al., 2020). In particular, chronologies for shallow shelf deposits still suffer from limited biostratigraphical resolution and global synchronization (Pekar et al., 2003). A change in water depth of tens of meters associated with a negative OIE of ∼1‰ reported from shallow shelf deposits in Alum Bay/UK can serve as an example. The OIE of that section being originally attributed to the MECO (Dawber et al., 2011) is now considered to postdate the MECO (Agnini et al., 2014; Edgar et al., 2020; Fornaciari et al., 2010; Villa et al., 2021).

1.1. Sea-Level Records From Shallow-Water Sediments

Continental margins and epicontinental sedimentary basins represent remarkable archives of the history of sea-level fluctuations and allow an independent test of reconstructions from the deep-sea record (Haq et al., 1988; Hardenbol et al., 1998; Vail et al., 1977). In addition to global controls, the sea-level record of these basins is influenced by local patterns of sediment accretion and vertical movements of the Earth's crust. These relative sea-level fluctuations are reflected in the stratigraphic record as a stack of repetitive sediment packages bounded by unconformities and their correlative conformities (sequence stratigraphy) (Haq et al., 1987; Vail et al., 1977). The primary sequence stratigraphic unit (third order depositional sequence) is characterized by its diagnostic internal architecture of stratigraphic terminations (onlap, downlap, toplap, truncation) and the systematic arrangement of shallowing upward cycles (parasequences or elementary sequences) within systems tracts (Lowstand Systems Tract [LST]; Transgressive Systems Tract [TST]; Highstand Systems Tract [HST]; Falling Stage Systems Tract [FSST]) (Catuneanu et al., 2011; Haq et al., 1987; Strasser, 2018). To separate local and global factors, compaction, loading, and water depth of the sediments are additionally considered (backstripping) (Kominz et al., 2008; Miller et al., 2005). Summary sea level curves of the long-term (first order: 50–100 Myr duration) and their superimposed short-term (third order: 0.5–5.0 Myr duration) variations are available for the entire Phanerozoic, that is, the last ∼540 Myr (Haq et al., 1987; Hardenbol et al., 1998; Miller et al., 2005, 2020; Peters et al., 2010), but low biostratigraphic resolution of shallow marine deposits hampers demonstrating the global nature of third order depositional sequences (Pekar et al., 2003).

A special feature of shallow marine carbonate platforms and ramps is the presence of laterally extensive, horizontally stratified beds being decimeters to a few meters thick that represent the shallow subtidal lagoon and tidal flat (Scholle et al., 1983). These beds normally show a shallowing-upward trend, which culminates along the top with a surface of subaerial exposure (Schlager, 1992). In this respect, these beds can be considered depositional sequences of the fourth order or lower hierarchical orders (elementary sequences) corresponding in the time-domain to the Milankovitch frequency band (Strasser, 2018). Vertical accretion of the elementary sequences being limited by sea level, their thickness represents a sensitive dipstick for the rate of formation of sedimentary accommodation space per sea level cycle and their stacking pattern for its long-term evolution (Read et al., 1995). Using corrections for basin subsidence, the eustatic component of the evolution of accommodation space can be inferred using Fischer plots (Fischer, 1964; Husinec et al., 2008; Read et al., 1995). The systematics of the bundling patterns of the accommodation evolution also provide clues to the completeness of a stratigraphic sequence and a formation in the climatic state of the Hothouse or Icehouse (Hardie & Shinn, 1986; Read et al., 1995). While the geological record of carbonate platforms from the Mesozoic Hothouse periods can be considered sufficiently complete for astrochronological calibrations (Strasser, 2018), orbital solutions for calibrations to the long-term motion of the Earth with proper phases of the eccentricity variations exist only for the last ∼50 Myr (middle Eocene) (Laskar et al., 2011). Astronomical time-scale synchronizations between Eocene records from the deep-sea and large perennial lakes have been presented recently (Shi et al., 2019; Westerhold et al., 2018), but no attempts have been made yet to astronomically calibrate Eocene shallow carbonate platforms or ramps (Martín-Martín et al., 2021), and to compare the records with global data. An example of a Middle Eocene carbonate ramp is the classic type area of the Lutetian Stage in the epicontinental basin of Paris (NW France) (Figure 1) (Mégnien & Mégnien, 1980; Merle, 2008). For this largely undeformed stratigraphic section, very detailed studies on bio- and sequence stratigraphy, fauna and flora, and sedimentary facies have been presented (Briais, 2015; Gély, 2016; Gély & Leroux, 2019; Haq et al., 1988; Merle, 2008) which can serve as a basis for an astrochronolgical calibration and comparison with sea-level data and proxy records from the deep sea.

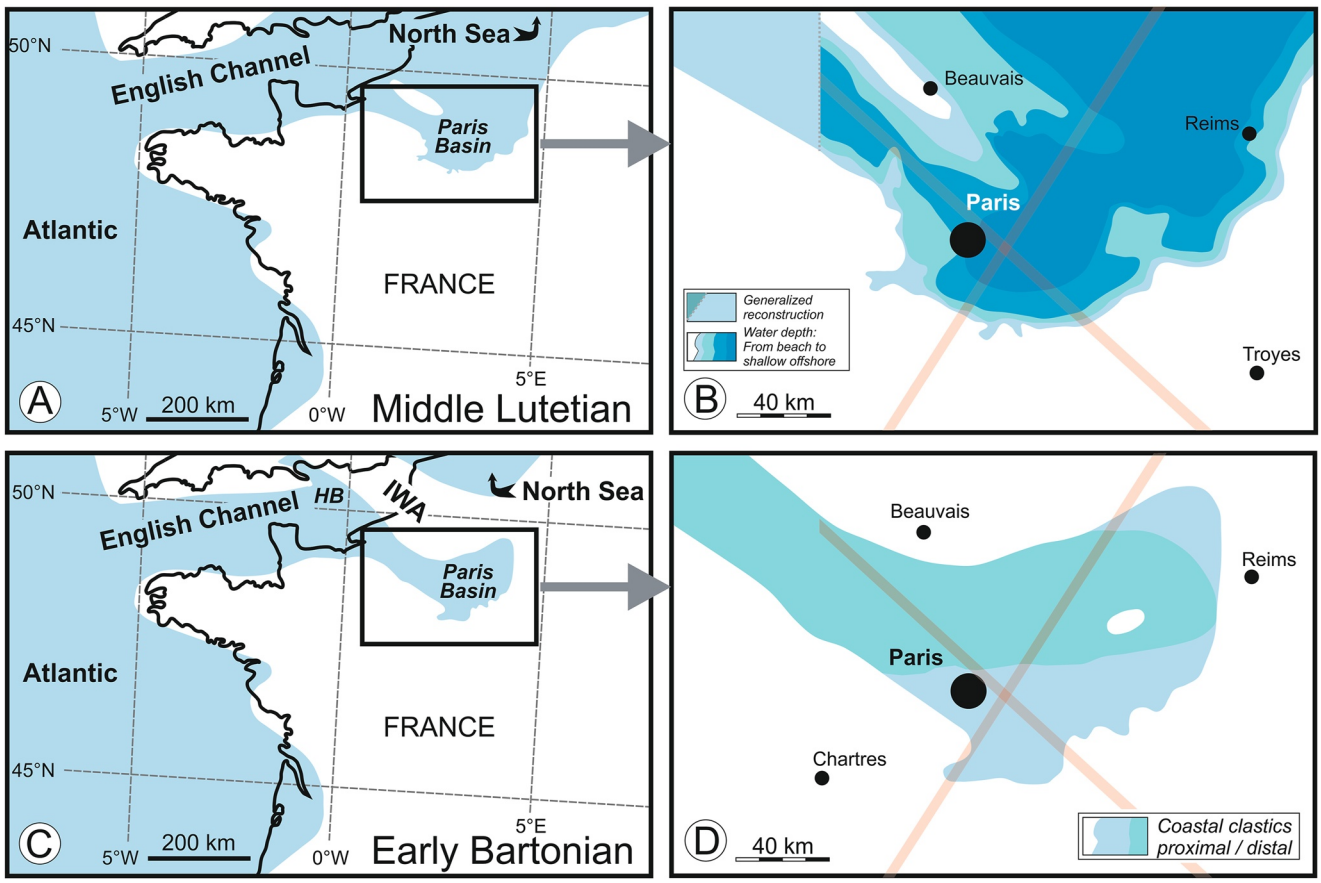

Figure 1. Paleogeographic sketch maps of NW-France (Paris basin) showing the distribution of marine facies during the middle Lutetian and early Bartonian. (a, c) Overview of the marine paleogeography of France during the middle Lutetian and early Bartonian, respectively. Inset shows the positions of the maps shown in (b) and (d). (b) Facies distributions of the Banc de Saint-Leu, elementary sequence #6 of Calcaire Grossier Moyen. (d) Facies distributions during the early Bartonian, elementary sequence #21 (Auversian Sand). Bold black lines: present-day coastline. Hypothetical river courses are not shown. The cross of orange lines shows the position of the transects used to construct the shoreline trajectory (Figure 3). HB, Hampshire Basin; IWA, isthmus of Weald-Artois. Redrawn from various sources (Barrier et al., 2018; Gély, 2016; Merle, 2008).

1.2. Approach

Based on a re-evaluation of available biostratigraphic (Aubry, 1983, 1985; Chateauneuf & Gruas-Cavagnetto, 1978; Steurbaut & Nolf, 2021) and sequence- and cyclostratigraphic stratigraphic data of the middle Eocene from Paris basin (PB), France (Briais, 2015; Gély, 2016; Gély & Leroux, 2019), we present the first astrochronologically calibrated sequence stratigraphic classification for shallow-water deposits. For the synchronization of this classification with astronomical solutions of long-term changes in Earth orbital parameters, we complement the biostratigraphic chronology with a diagnostic, hierarchical system of small- and large-scale sedimentary cycles. Within this framework, we hypothesize the elementary sequences to represent the 0.405 Myr cycle of orbital eccentricity and the overarching depositional sequences (third order sequences) the 2.4 Myr cycle of eccentricity (Laskar et al., 2011; Westerhold et al., 2020). For this purpose, we present a reconstruction of the long-term evolution of the shoreline trajectory and sedimentary accommodation space of the shallow marine sediments using spatio-temporal changes in facies distributions and a Fischer Plot. We discuss the causes of similarities and differences of our reconstruction with glacioeustatic sea-level fluctuations inferred from $\delta^{18}O$ cycles of the deep-sea record. Our study provides evidence for small amplitudes of third order sea-level changes <10 m in concert with orbital insolation, but a strong, eustatic sea-level pulse of ≥30 m during the MECO unrelated to insolation forcing. In the light of a drop in surface ocean pH of ~0.2 during the MECO (Henehan et al., 2020) and spectacular skeletal preservation of many PB fossils (Brachert et al., 2022; Merle, 2008), our findings suggest the PB record to be highly suited as a natural laboratory for future studies on the effects of ocean warming and acidification on skeletal calcification patterns of shallow marine biota.

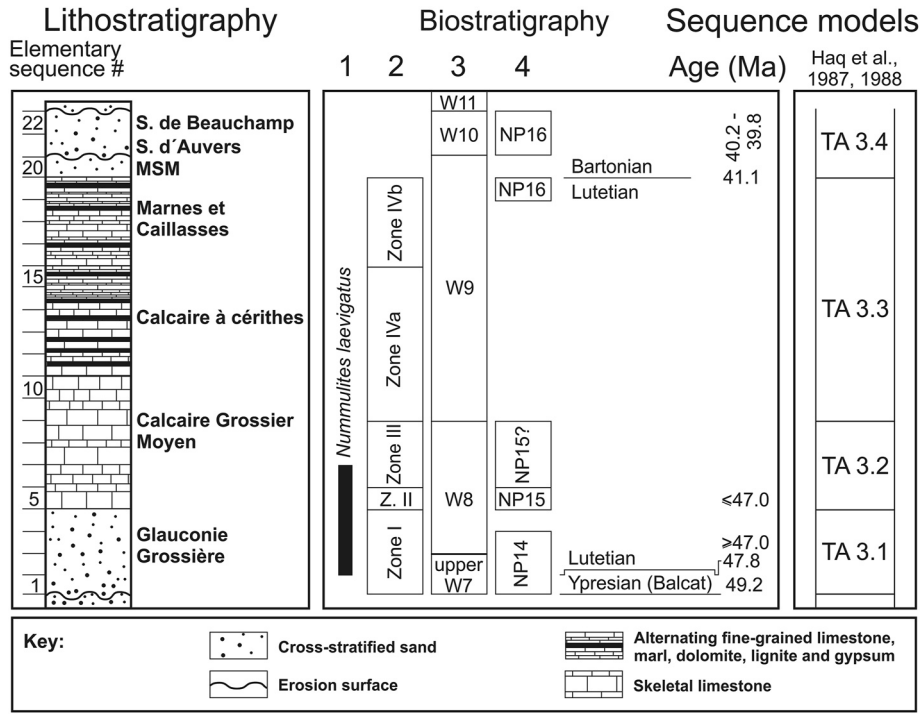

Figure 2. Biostratigraphy of the Lutetian (including late Ypresian) and early Bartonian in Paris basin (PB). Left box: Lithostratigraphy (MSM, Sables de Mont-Saint-Martin) (Blondeau, 1965; Gély, 1996; Merle, 2008). Middle box: Biostratigraphy. 1: Distribution of *Nummulites laevigatus* (Merle, 2008), 2: macrofossil data (Abrard, 1925), 3: Dinoflagellates (Chateauneuf & Gruas-Cavagnetto, 1978), 4: Nannoplankton (Aubry, 1983, 1985). Right box: Sequence stratigraphy for PB (Haq et al., 1987, 1988). Estimated ages from biostratigraphy calibrated according to CENOGRID timescale (Westerhold et al., 2020). Vertical scale is the number of elementary sequences, that is, time, to be compatible with Figure 3. See Supporting Information S1 for detail.

1.3. Middle Eocene Paleogeography, Paleoenvironments and Stratigraphy of the Classical Lutetian Type Region, Northwest France

Around the early/middle Eocene, the northwest European continent then located at ~45°N paleolatitude became flooded from the NE Atlantic and North Sea areas southward, forming a shallow marine gulf that extended several 100 km inland into the PB during its maximum extensions in the middle Lutetian and again in the early Bartonian (Gély, 2016; van Hinsbergen et al., 2015) (Figures 1 and 2). Flooding of the PB started in the latest Ypresian (Steurbaut & Nolf, 2021) and left behind glauconite-rich sand and larger foraminifer limestone (Glauconie Grossière [GG] showing signs of storm activity and intermittent sediment starvation (Gély & Leroux, 2019; Merle, 2008) (Figure 2). During the Lutetian, the GG was replaced by coarse skeletal carbonates of the Calcaire Grossier s.s. (CG Moyen). The single beds of the CG Moyen show great lateral continuity, characteristic facies and physical properties within the entire basin, so they were given individual names early on by medieval quarrymen (Merle, 2008). A peak of marine shallow-subtidal development was reached during the middle CG Moyen (Banc des Saint-Leu, Banc à vérins et du Vergelé, Couches des Lambourdes), when seagrass beds developed with a highly diverse and individual-rich fauna of larger benthic foraminifers (e.g., *Nummulites*, *Orbitolites*), thick-shelled and large-bodied mollusks (e.g., *Campanile giganteum*), sea urchins, fishes, and reef corals (e.g., *Acropora*, *Porites*, *Astreopora*) (Gély & Leroux, 2019; Merle, 2008; White, 2013). Although the diversity of reef corals was quite high (≥9 genera), no true reefal frameworks were formed (Mégnien & Mégnien, 1980; Wallace & Rosen, 2006; White, 2013). Finally, in the late CG Moyen, lagoonal and freshwater systems became increasingly important, both, onlapping further landward and prograding basinward (Gély & Leroux, 2019; Merle, 2008).

During the formation of the CG Supérieur (CGS; or Marnes et Caillasses), the connection to the North Sea basin was increasingly lost as a result of tectonic uplift in the northern reaches of the basin forming the isthmus of Weald-Artois of the Bartonian (Barrier et al., 2018; Merle, 2008) (Figure 1). A continuous connection to the Northeast-Atlantic and fully marine subtidal conditions during the late Lutetian prevailed only in the

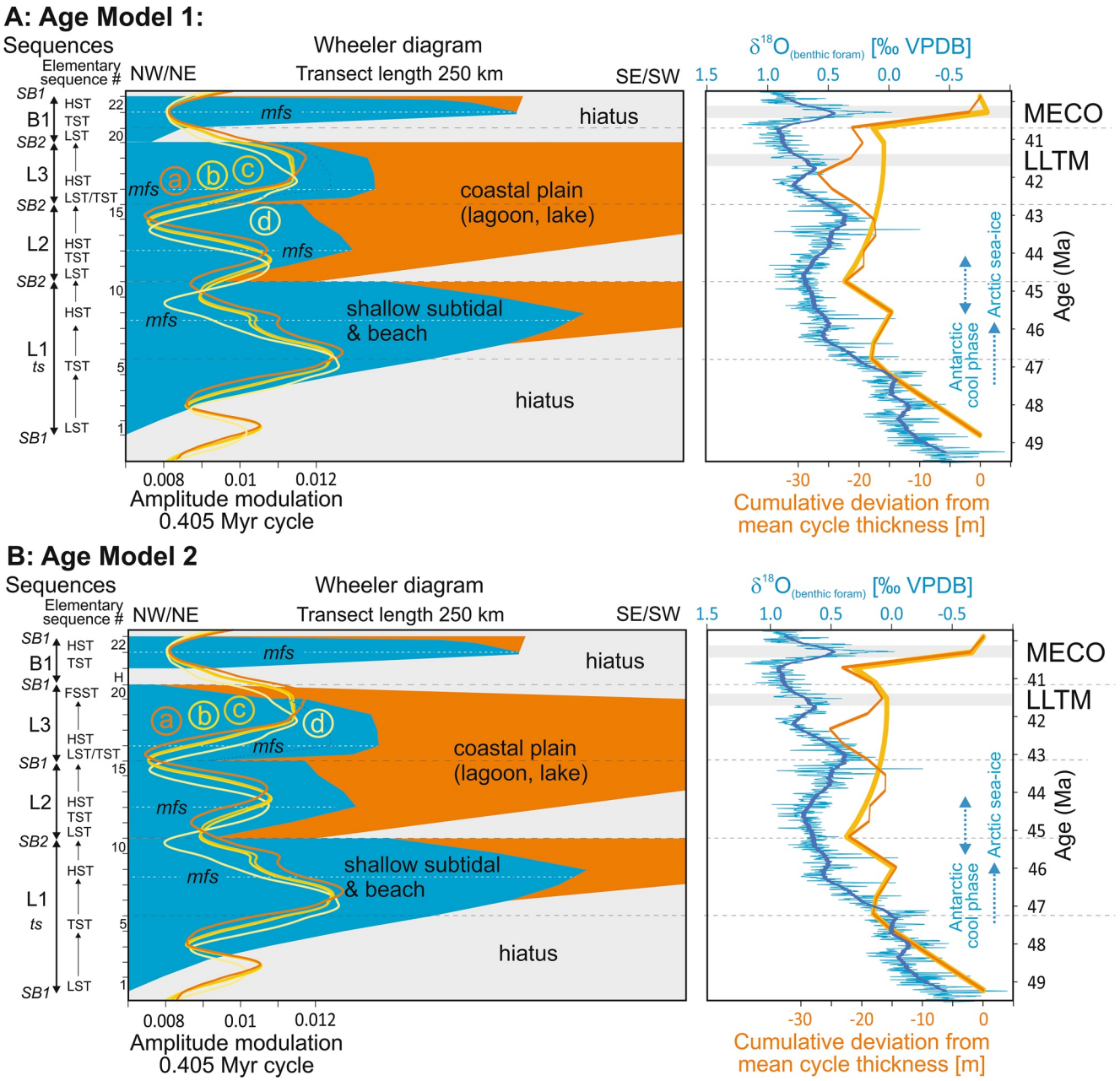

Figure 3. Sequence stratigraphy (third order) for the shallow marine and terrestrial deposits of the Paris basin for two separate age models. Left box: Sequence stratigraphy (Wheeler diagram). The spatiotemporal distribution pattern of the boundary between shallow marine deposits (blue) and lagoonal and terrestrial deposits (orange) approximates the shoreline trajectory. Model 1 is based on the classical three-systems-tracts approach (van Wagoner et al., 1988), where elementary sequence #20 represents the lowstand position of sequence B1 (variant 1 see text for details). In model 2, we adopted the concept of four systems tract sequence stratigraphy for sequence L3 (Catuneanu et al., 2011), where elementary sequence #20 represents the Falling Stage Systems Tract of the L3 sequence (variant 2 see text for details). The dotted line in L3 shows the trajectory for the NW-SE transect. Partial erosion of L2 and L3 due to localized uplift of the isthmus of Weald-Artois prior to B1 is not shown (Gély, 1996). H, non-depositional hiatus. Overlay curves over Wheeler diagram: Amplitude of the long eccentricity cycle (solutions a, b, c, d drawn in orange to yellow colors) (Laskar et al., 2011). Right box: Astronomically dated record of deep-sea benthic foraminifer $\delta^{18}O$-values (blue) (Westerhold et al., 2020). Thick blue line shows running mean over 405 Kyr (duration of long eccentricity cycle) for $\delta^{18}O$. Note inverted scale for the $\delta^{18}O$-values in order to highlight the similarity with the shoreline trajectory. Blue dotted arrows show the approximate onset of SSTs cool enough for the formation Arctic sea-ice (Stickley et al., 2009) and Antarctic cool phase (Cramwinckel et al., 2018). Right Plots show the cumulative deviation of the thickness of the individual elementary sequences from their mean thickness, for decompacted/compacted raw data (thick yellow line) and modeled decompacted/compacted data for L2 and L3 (thin orange line; see text for details).

northwestern section of the basin, while most parts of the remaining basin were now occupied by extensive beaches, lagoons, and lakes leaving behind small-scale alternations of sand, limestone, dolomite and lignite or evaporite (Merle, 2008) (Figure 2). Due to localized uplift, the stratigraphic contact of the CGS is only locally conformable and continuous with laguno-marine sand of the Sables de Mont-Saint-Martin assigned to the early Bartonian (Gély, 2016; Merle, 2008). This unit is covered by a widely distributed package of shallow marine sand (Sables d'Auvers, Faluns de Guépelle) and marine-brackish to terrestrial sand (Sables de Beauchamp) that rests conformably on top of the Sables de Mont-Saint-Martin, but unconformably on a substrate formed by CGS or even CG Moyen in some areas of PB (Gély, 2016; Merle, 2008). The well-sorted, mostly cross-bedded sands, calcarenites, and shell beds rapidly spread for several 100 km along a narrow corridor from the Atlantic Ocean landward to the SW (Figures 1d and 2). A highly diverse fossil fauna with very abundant small and larger benthic foraminifers, bryozoans, mollusks, echinoids, crustaceans, together with calcareous green algae (Dasycladaceae) documents a shallow-water environment with extensive seagrass beds with ≤10 m depth (Gall, 1983). A diverse reef coral association (≥9 genera, e.g., *Astreopora*, *Goniopora*, *Acropora*), again without evidence of reefal frameworks, documents a new phase of colonization of the gulf by reef corals (Brachert et al., 2022; Gall, 1983; Mégnien & Mégnien, 1980; Wallace & Rosen, 2006; White, 2013).

1.4. Biostratigraphy

A characteristic of all of the shallow-marine to terrestrial deposits of PB is a regular, vertical stacking of shallowing upward sequences (Briais, 2015; Gély & Leroux, 2019), referred to as elementary sequences *sensu* Strasser (2018) that we numbered #1 to #22 (Figure 2). For the classic Lutetian of PB three separate biostratigraphic classifications have been proposed (Merle, 2008) (Figure 2): (a) a largely local system of five zones based on shallow-marine benthic macrofauna (Abrard zonation) (Abrard, 1925), (b) a classification using the first and last occurrences of dinoflagellate cysts (W-zonation) (Chateauneuf & Gruas-Cavagnetto, 1978), and (c) calcareous nannoplankton stratigraphy (NP-zonation) (Aubry, 1983, 1985; Gradstein et al., 2020; Martini, 1971; Steurbaut & Nolf, 2021). Based on these biostratigraphic classifications, the GG, CG and Sables d'Auvers together with Sables de Beauchamps can be dated latest Ypresian to early Bartonian (Figure 2). Estimated ages from biostratigraphy were calibrated according to GTS2020 (Gradstein et al., 2020) and the CENOGRID timescale (Westerhold et al., 2020). See Supporting Information S1 for detail.

2. Materials and Methods

We use the concept of sequence stratigraphy, including terms and abbreviations in their original form (systems tracts and major stratigraphic surfaces in upper case, minor surfaces in lower case letters), and concepts as revised by subsequent work (Catuneanu et al., 2011). Based on a series of detailed lithological maps for nine time slices of the Lutetian and two time slices of the Bartonian (Gély, 2016; Merle, 2008), the distribution of marine-subtidal and continental deposits (including beach and lagoonal facies) was recorded along two transects in a NW-SE and NE-SW direction, respectively (Figure 2). For the elementary sequences of the GG and the "Pierre à liards," only the transect in NE-SW direction was used due to the paleogeographic evolution of the basin, for all other units both transects were used and missing data interpolated; the location of the transects was chosen to be as close as possible to the two neostratotype sections St. Vaast-les-Mello and St. Leu-d'Esserent (Pomerol, 1981) termed "historical stratotype" by Steurbaut and Nolf (Steurbaut & Nolf, 2021). No distributional map for the Couches des Lambourdes elementary sequence (#8) is available; its distribution in the transect is shown semi-quantitatively (from Merle, 2008). Also for sequences L2 and L3, no maps for each individual elementary sequences are available except for maps showing the maximum flooding stage; the corresponding flooding pattern and shoreline trajectory were adopted from previous work and calibrated for Figure 3 using the facies maps available for L2 and L3 (Gély, 1996, 2016; Gély & Leroux, 2019; Gély & Lorenz, 1991).

In carbonate sedimentology the long-term control behind thickness variations of cyclically built, shallow-marine sedimentary sequences is graphically solved by Fischer plots (Husinec et al., 2008; Sadler et al., 1993). For constraining estimates of third order sea-level changes, we have used Fischer Plots (Husinec et al., 2008; Sadler et al., 1993) (Figures 3 and 4). In the diagrams, we plotted the elementary sequence number/astrochronological age on the *X*-axis, and the cumulative deviation from the mean thickness of the individual elementary sequences corresponding to a cycle on the *Y*-axis, thus recording long-term deviations of accommodation space from mean subsidence, for example, deviations from mean due to eustatic sea level fluctuations (Husinec et al., 2008; Sadler et al., 1993).

Thickness data for the individual elementary sequences was taken from the literature (Mégnien & Mégnien, 1980; Merle, 2008) (Table 1). For the CG Supérieur (L2, L3) this thickness information is not systematically available elementary sequence by elementary sequence. In those cases we have considered proportionally the mean thickness for the elementary sequences of this formation (Merle, 2008). In order to obtain an estimate of the magnitude of the variations in accommodation space during the formation of depositional sequences L2 and L3, we modeled the thicknesses of the individual elementary sequences. For this purpose, we kept the total thickness of the third order sequences and number of elementary sequences per depositional sequence constant, but assumed a thinning-upward trend of the elementary sequences (Figures 3 and 4).

Fischer Plots do not take into account any compaction effects and in this respect do not allow for a quantitative reconstruction of the evolution of accommodation space (Husinec et al., 2008). To achieve a realistic representation of changes of accommodation space using a Fischer Plot, we implemented a decompaction/compaction procedure (van Hinte, 1978). In a first step, all rocks were decompacted to their original thickness according to a maximum overburden of 200–300 m in the center of the basin (Brigaud et al., 2020) using decompaction numbers between 1.05 and 2.0 depending on lithology (Goldhammer, 1997) (Table S1 in Supporting Information S1). For the Fischer plots, decompacted thickness of the individual elementary sequences was progressively compacted, elementary sequence by elementary sequence, with increasing burial. For a thickness of ∼100 m of the studied sequence, we assumed no compaction has taken place for lithologies with a decompaction number = 1.05 (Goldhammer, 1997). For lithologies with a decompaction number = 2, we assumed a quasi-linear relationship between burial depth and degree of compaction according to Equation 1

$$C = (Z + 130.08)/130.08 \quad (1)$$

where C is the compaction number and Z is burial depth in meters (Goldhammer, 1997) (Figure S4 and Table S1 in Supporting Information S1). For the substrate rocks, no decompaction/compaction effect was taken into account.

3. Results and Discussion

3.1. Sequence Stratigraphy

Four large-scale depositional sequences (third order depositional sequences) (Haq et al., 1987; Vail & Mitchum, 1977) are distinguished by this study in the late Ypresian to early Bartonian deposits of PB, three of them in the latest Ypresian-Lutetian (L1–L3) (Gély, 1996; Merle, 2008; Steurbaut & Nolf, 2021) and one in the lower Bartonian (B1) (Figure 2). Characteristic of the sequences is a systematic internal structuration by shallowing upward cycles, each up to several meters thick (Table 1). The shallowing upward cycles topped by surfaces of subaerial exposure in most examples are interpreted as elementary sequences that are a typical feature of shallow carbonate platforms and ramps (Gély & Leroux, 2019; Strasser, 2018). The third order depositional sequences described here are heterogeneous in terms of the number of underlying elementary sequences (Gély, 1996) (Table 1, Figure 3); for practical reasons, we use the classical model of depositional sequences with three system tracts for this study and refrain from using alternative, more refined models (Catuneanu et al., 2011; van Wagoner et al., 1988). For previous sequence and cyclo stratigraphic work, the reader is referred to the literature (Briais, 2015; Briais et al., 2016; Gély, 1996, 2016; Gély & Lorenz, 1991; Haq et al., 1987, 1988; Hardenbol et al., 1998; Merle, 2008) (Figure 2).

Depositional sequence L1 is formed by a set of 10 elementary sequences (Gély, 1996; Gély & Leroux, 2019) (Figure 3, Table 1). The elementary sequences #1 to #4 representing the GG are restricted to the most distal, northernmost, parts of the basin and document the incipient, successive south- and southeastward flooding of PB from the English Channel and North Sea (Figures 1 and 3). The subsequent elementary sequences #5 to #10 of the CG Moyen each successively onlap further southward and southeastward into the basin. Maximum landward geographic distribution of marine facies, several 100 km southeastward, is reached with elementary sequence #8 of the Couches des Lambourdes (maximum flooding) (Merle, 2008). The next younger elementary sequences, #9 (Banc vert 1) and #10 (Banc vert 2), show an even wider overall landward distribution than the previous ones (maximum landward shift of coastal onlap), but the marine facies are now restricted to the northwestern part of the basin only. In agreement with previous studies (Gély, 2016; Gély & Lorenz, 1991), we interpret this stacking pattern as the expression of the lowstand position (LST) (elementary sequences #1 to #4), Transgressive Systems

Paleoceanography and Paleoclimatology

10.1029/2023PA004633

Table 1
Lithostratigraphy of the Middle Eocene in Paris Basin (Blondeau, 1965; Gély, 1996)

Lithostratigraphy	Name of sub-unit	Elementary sequence # (Paraseq. of Gély, 1996)	Thickness (m) (modeled, this study)	Nannoplankton biostratigraphy (Aubry, 1983)	W-Zonation (Chateauneuf & Gruas-Cavagnetto, 1978)	Sequence	Systems tracts	Age model 1 (Ma) (basal age of parasequence)	Age model 2 (Ma) (basal age of parasequence)	Decompaction number	Comments
Calcaire grossier inférieur	Glauconie Grossière	1 (A1)	1.0	Upper NP14	W7	L1	LST	48.8	49.2	1.05	Equivalent of Sables de Chaumont-en-Vexin, BALCAT event (Steurbaut & Nolf, 2021)
		2 (A2)	1.0		W7	L1	LST	48.4	48.8	1.05	Occurrence of *Nummulites laevigatus*
		3 (A3)	1.0	NP14	W7	L1	LST	48.0	48.4	1.05	
		4 (A4)	1.0		W7	L1	LST	47.6	48.0	1.05	
	Pierre à liards, Banc à mollusques	5 (A5)	2.0	NP15	?	L1	TST ts	47.2	47.6	1.05	
Calcaire grossier moyen	Banc de Saint-Leu	6 (A6)	5.0		W8	L1	TST	46.8	47.2	1.05	
	Banc à vérins	7 (A7)	6.0		W8	L1	TST	46.4	46.8	1.05	
	Lambourdes, Vergelé	8 (A8)	6.0		W8	L1	TST/HST mfs	46.0	46.4	1.05	
	Banc vert inférieur	9 (A9)	0.5		W9	L1	HST	45.6	46.0	2.0	
	Banc vert supérieur	10 (A19)	0.5		W9	L1	HST	45.2	45.6	2.0	
Calcaire grossier supérieur	Calcaire à cérithes	11 (B1)	3.3[a] (4.0)		W9	L2	LST/ts	44.8	45.2	1.05	
		12 (B2)	3.3[a] (5.0)		W9	L2	TST	44.3	44.8	2.0	
		13 (B3)	3.3[a] (3.8)		W9	L2	HST	43.9	44.3	2.0	
		14 (B4)	3.3[a] (2.7)		W9	L2	HST	43.5	43.9	2.0	
	Rochette	15 (B5)	3.3[a] (1.6)		W9	L2	HST	43.1	43.5	2.0	
	Marnes et Caillasses inférieures										
	Marnes et Caillasses supérieures	16 (C1)	3.3[a] (1.5)	Lower (but not basal) NP16	W9	L3	LST/TST	42.7	43.1	1.05	Falun de Foulangues (Cavelier & Le Calvez, 1965), Calcaire à *Styloc[a]oenia monticularia* (Merle, 2008)
	Marnes et Caillasses supérieures	17 (C2)	3.3[a] (6.3)		W9	L3	HST	42.3	42.7	2.0	Falun de Foulangues (Cavelier & Le Calvez, 1965)
	Marnes et Caillasses supérieures	18 (C3)	3.3[a] (4.5)		W9	L3	HST	41.9	42.3	2.0	Falun de Foulangues (Cavelier & Le Calvez, 1965)
	Marnes et Caillasses supérieures	19 (C4)	3.3[a] (1.0)		W9	L3	HST	41.5	41.9	2.0	Falun de Foulangues (Cavelier & Le Calvez, 1965)
											Late Lutetian Thermal Maximum (LLTM) (Westerhold et al., 2017)
Auversien	Sables de Mont-Saint-Martin	20	4.0	NP16	W9	B1/L3	LST/FSST	41.1	41.5	1.05	FSST (age model 2 & 4: hiatus between parasequences #20 and #21)
	Sables d'Auvers	21	30.0	NP16	W10	B1	TST	40.7	40.7	1.05	MECO
	Sables de Beauchamp	22	8.0	NP16	W10	B1	HST	40.3	40.3	1.05	MECO

Note. Elementary sequences according to Gély in Merle (Gély & Leroux, 2019; Merle, 2008), modified for Bartonian parasequences (Briais, 2015). Thickness (Cavelier & Le Calvez, 1965; Mégnien & Mégnien, 1980; Merle, 2008) and decompaction number (Goldhammer, 1997) from literature.

[a]Averaged over total thickness of unit.

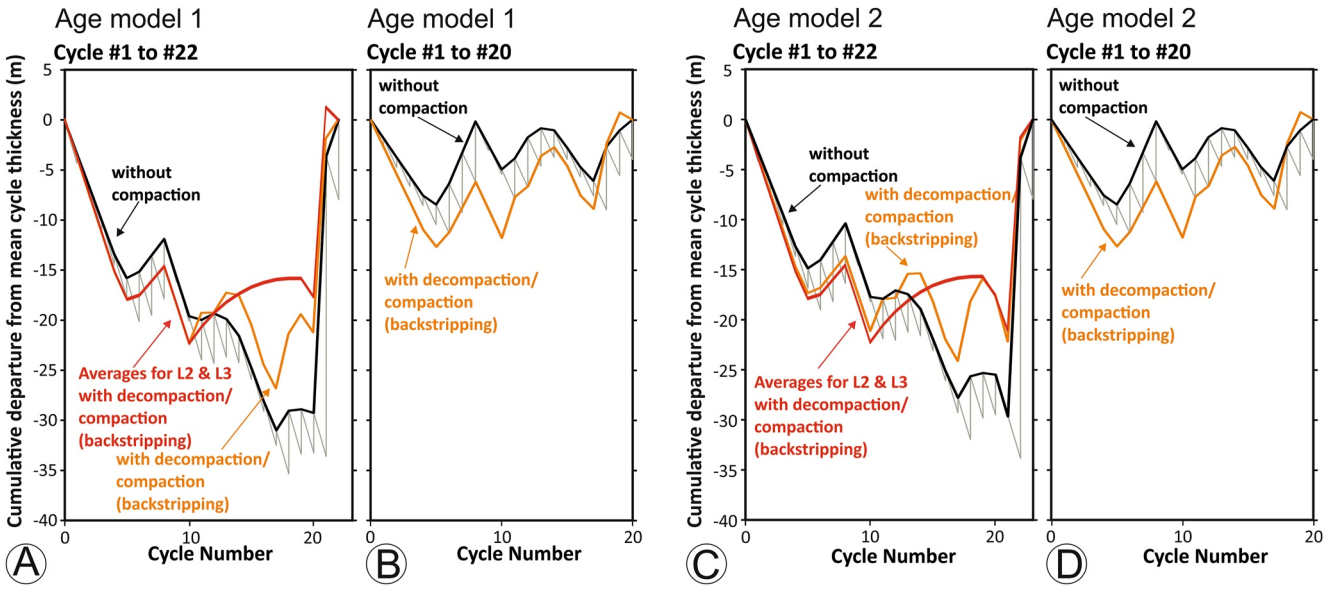

Figure 4. Fischer plots for the middle Eocene shallow-marine record of Paris basin (France) demonstrating the effect of the time-window selected for the long-term pattern. (a, b) Fischer plots based on age model 1 for cycles #1 to #22 (a) and #1–20 (b), respectively. (c, d) The same of for age model 2. The black and gray lines in all diagrams show a classical Fischer Plot constructed with a pre-formatted excel spreadsheet (Husinec et al., 2008). The red and orange graphs were constructed using a decompaction/compaction procedure (backstripping) (van Hinte, 1978) on average thickness for elementary sequences of L2 and L3 sequences. Black and orange lines show trends for modeled thicknesses for elementary sequences of L2 and L3 (Supporting Information S1).

Tract (TST) (#5 to #8) and Highstand Systems Tract (HST) (#9 and #10) of a single third order depositional sequence. In this context, the prominent shell beds of elementary sequence #5 (Banc à mollusques, Pierre à liards) represent the transgressive surface (ts) of the basal TST (van Wagoner et al., 1988). In contrast to a previous study, the maximum flooding surface (mfs) at the top of the TST is not placed at the base of Couches des Lambourdes elementary sequence #8 (Haq et al., 1988), but inside the Couches des Lambourdes that is considered by us as the physical expression of the mfs within PB (van Wagoner et al., 1988). In this sense, the absence of any evidence for a downlapping geometry associated with the mfs within the basin represents the expression of an aggradational geometry of a laterally extensive carbonate factory expressed by the "bancs" of the classical stratigraphic classification that each accounted for a complete filling of accommodation space available within the entire basin.

The lower boundary of the L1 sequence is an inter-regionally distributed erosional unconformity, interpreted in this study as sequence boundary type 1 (SB1) (van Wagoner et al., 1988). Unlike the lower boundary of L1, no erosional features are evident at the contact of L1 and L2. For that reason, this boundary is considered a type 2 sequence boundary (SB2) (van Wagoner et al., 1988). Localized, incised channels truncating the top of elementary sequence #8 near the Vigny Anticline reflect synsedimentary uplift (Blondeau, 1965).

The L2 and L3 sequences representing the CGS are also taken as third-order depositional sequences being made up of 5 and 4 elementary sequences, respectively (Gély, 1996; Gély & Leroux, 2019). However, little information is available regarding the thickness and spatial distribution of the individual elementary sequences, except for the stage of maximum flooding (Gély, 2016; Merle, 2008) or specific marker beds (Cavelier & Le Calvez, 1965; Gély & Leroux, 2019) (Table 1). Since there is no conspicuous erosional surface between L2 and L3 (Gély, 2016; Gély & Lorenz, 1991), this stratigraphic contact represents a SB2. An intercalation of marine sand and limestone containing reef corals (*Stylocoenia monticularia*) (Cavelier & Le Calvez, 1965) and other marine immigrants (*Discorinopsis kerfonei*, *Linderina brugesi*) of Falun de Foulangues (Aubry, 1983) is considered the mfs of the L3 depositional sequence rather than the mfs of a T/R cycle encompassing the entire CGS (L2 and L3) (Briais, 2015; Merle, 2008) (Table 1). Originally, its stratigraphic position was reported from the top of the CGS (Cavelier & Le Calvez, 1965) and assigned to the latest Lutetian, but the stratigraphic position of the Falun de Foulangues with Calcaire à *Stylocoenia monticularia* within CGS is not fully resolved yet (Gély, 1996; Merle, 2008) (Figure 1, Table 1).

The basal contact of the early Bartonian depositional sequence (B1) is gradual and conformable for very localized occurrences of shallow-marine to lagoonal sand of elementary sequence #20 (Sables de Mont-Saint-Martin), but

discontinuous and erosional for basin-wide distributed shallow-marine sand of elementary sequence #21 (Sables d'Auvers) that is separated from both, elementary sequence #20 and L3 by an erosional unconformity including karst formations (Briais, 2015; Merle, 2008). No information is available, as to the geometry of this erosional surface, that is, whether it has the form of an incised valley related to fluvial erosion formed during forced regression, or is essentially planar and related to shoreline ravinement during marine transgression. The latter is reflected by bivalve borings in limestone along the stratigraphic contact and within pebbles reworked from the substrate. In terms of classical three systems tracts sequence stratigraphy (Catuneanu et al., 2011), elementary sequence #20 has a LST geometry associated with a basal SB2 and topped by a ravinement surface (ts) making it part of the B1 sequence (Figure 3). Alternatively, elementary sequence #20 may be considered the very late HST, or in terms of four systems tracts sequence stratigraphy FSST (Catuneanu et al., 2011), because it is erosionally truncated along its top (SB1) and, therefore to be considered part of the L3 sequence (Figure 3). Thus, depending on the model, the eustatic minimum of sea-level is to be placed chronostratigraphically within elementary sequence #20 or above, implying in the latter scenario a subaerial hiatus. In the absence of additional data, we refer to these two variants in parallel below. In variant 1, we draw the L3/B1 boundary as SB2 according to three systems tracts model (no hiatus) and consider elementary sequence #20 as LST of the B1 sequence. In variant 2, we consider elementary sequence #20 as late HST (or FSST) (Catuneanu et al., 2011) of the L3 sequence being truncated at its top by a SB1 and assume a hiatus between L3 and B1, that is, spatial coincidence of the sequence boundary and transgressive surface. The subsequent Sables d'Auvers and Sables de Beauchamp where classified as individual elementary sequences #21 and #22 because of a freshening upward trend and/or local paleosol cap in both (Briais, 2015). The B1 sequence is thus formed of only two (variant 2) or three (variant 1) shallowing upward cycles interpreted to represent elementary sequences; a respective subaerial exposure at the top is well documented for elementary sequence #20 by an erosional top and elementary sequences #21 and #22 by freshwater limestone, paleosols and eolian deposits, respectively (Briais, 2015; Gély, 2016) (Table 1). With regard to the rapid landward shift of marine facies in elementary sequence #21 associated with coastal ravinement, and subsequent rapid basinward progradation of brackish and eolian sand as well as freshwater limestone at the top of elementary sequence #22, the stack of two elementary sequences is interpreted as TST, mfs, and HST of a complete third order depositional sequence (Gély, 2016; Haq et al., 1988). Eolian reworking of previously formed marine sand and prograding freshwater limestone at the top of the unit documents a renewed, rapid sea-level fall. Maximum flooding of the basin expressed by the spatial distribution of marine facies closely matched that of the L1 sequence and substantially exceeded marine flooding of the basin during L2 and L3 (Figure 3).

3.2. Age Model

For the age model, we use biostratigraphic datums as tie-points for a comparison of the PB record with global data sets of $\delta^{18}O$ and eustatic sea-level (Miller et al., 2020; Westerhold et al., 2020). Using a cyclostratigraphical approach, the basal age of the GG (elementary sequence #1) was estimated 47.8 Ma (Briais et al., 2016). In contrast, a calcareous nannoplankton association from the basal deposits of the classical Lutetian in the northern PB attributed to the global BALCAT-event of latest Ypresian age documents a basal age of 49.2 Ma for elementary sequence #1 (Steurbaut & Nolf, 2021; Westerhold et al., 2020) (Figure 2 and Figure S2 in Supporting Information S1). The latter finding is consistent with the first occurrence of *Nummulites laevigatus* being a biostratigraphic marker of the lower Lutetian (Gradstein et al., 2020) in elementary sequence #2, which is why we place the Ypresian/Lutetian (Y/L) boundary between elementary sequences #1 and #2. Chronostratigraphically, the Y/L boundary is equivalent with magnetochron C21r/C21n (Westerhold et al., 2020) or intra-C21r (Molina et al., 2011), that is, according to CENOGRID (Westerhold et al., 2020) 47.8 or ∼48.5 Ma (Figure 2). Nannoplankton data show that elementary sequences #3 to #5 approximate the NP14/NP15 boundary, that is, "middle" of C21n (Molina et al., 2011) with a CENOGRID age of ∼47.0 Ma (Westerhold et al., 2020), whereas elementary sequences #21 and #22 representing NP16 (pars) and W10, respectively, can be placed within C18n.2n (Gradstein et al., 2020) and dated 40.3–39.8 Ma according to the CENOGRID timescale (Westerhold et al., 2020). The next marine units above were ascribed biostratigraphically to W11 and are <39.8 Ma (Chateauneuf & Gruas-Cavagnetto, 1978; Westerhold et al., 2020) (Figure 2). On this basis, elementary sequences #21 and #22 were ascribed to the MECO, centered at ∼40.3 Ma (Westerhold et al., 2020), while the Lutetian/Bartonian boundary is placed between elementary sequences #19 and #20 (Gély, 1996; Merle, 2008); according to the CENOGRID time-scale this boundary is positioned within magnetochron C19n and dates 41.1 Ma (Westerhold et al., 2020).

For a test of the age model, we compare the sequence architecture of PB with reconstructions of global sea-level fluctuations based on deep-sea data and an astronomically calibrated $\delta^{18}O$ data set (Miller et al., 2020; Westerhold et al., 2020), because the sea-level record has no consistent astrochronology in the middle to late Eocene. In this context, we interpret the biostratigraphically-fixed surfaces of deep erosion and karstification at the base of the L1 and B1 sequences (Briais, 2015) as the result of forced regression (SB1), and the ravinement (ts) at the base of elementary sequence #21 as the result of rapid transgression (Catuneanu et al., 2011), both related to suprar-egional sea-level fluctuations (Figures 2 and 3). We further consider the two striking global minima of sea-level at the base and top of the classical Lutetian as well as the subsequent MECO maximum (Miller et al., 2020) as global equivalents of the PB record (Figures 2 and 3). With regard to the age calibration, we use the astrochron-ologically dated CENOGRID data set of $\delta^{18}O$ (Westerhold et al., 2020) rather than the sea-level reconstruction (Miller et al., 2020). According to these constraints, the base of L1 dates ∼49 million years (Ma), the base of B1 40.6 Ma and the surface of maximum marine flooding (mfs) of B1 40.3 Ma (Westerhold et al., 2020) (Table 1). Using these datums and assuming a gapless sedimentary record (i.e., no elementary sequence missing) across the SB2 boundaries of the three L sequences, or 21 elementary sequences (Table 1) we come up with a total duration of ∼8.7 Myr for the entire stack of 22 elementary sequences. Thus, the individual sequences each accounted for an average of ∼2.2 Myr and the elementary sequences for ∼0.41 Myr, respectively. Given the possibility of hiatuses, a mean duration of 0.41 Myr of the elementary sequences could well correspond to the long eccentricity cycle of the earth's orbit with a duration of 0.405 Myr and the average duration of the third order sequences with that of the very long eccentricity cycle of ∼2.4 Myr (Laskar et al., 2011). Below, we discuss why a pacemaking effect of long and very long eccentricity cyclicity for the elementary and third order depositional sequences inferred from the total duration of the record and number of sequences is likely not coincidental. For this purpose, we use the La2011 (Laskar et al., 2011) solution in this study as it is the most accurate solution and other solutions available are not an improvement to La2011 for the time interval we studied. First of all, the number of elementary sequences differs among the third order sequences, consistent with the long-term pattern of the astrochronologically tuned global $\delta^{18}O$ record and orbital solution (Laskar et al., 2011; Westerhold et al., 2020) (Figure 3). According to the long-term deep-sea $\delta^{18}O$ pattern, we date the boundary for L1/L2 as 44.5 Ma, for L2/L3 as 42.1 Ma and for L3/B1 as 40.6 Ma (Westerhold et al., 2020). In contrast, when assuming the elementary sequences reflect a forcing by the long-eccentricity cycle, we derive datings using cycle counts of 45.0 Ma for L1/L2, 42.9 Ma for L2/L3 and 41.3 Ma for L3/B1 (Figure 2, Table 1). While our age assignments for L1/L2 using the long-term pattern of the deep-sea record and cycle counts gives consistent results, the datums for L2/L3 and L3/B1 differ by the duration of 2 and 1 cycles of long eccentricity, respectively. Since the cycle counts give older ages, a hiatus at the L2/L3 and/or L3/B1 boundaries is conceivable, although the SB2s document conformable contacts. Rather, the discrepancy in the age estimate of the L2/L3 and L3/B1 boundaries represents an artifact of the methodological approaches: while the isotope pattern provides minima/maxima as tie points that corre-spond to eustatic sea level maxima/minima, sequence boundaries represent periods of maximum rate of sea-level fall between sea-level maxima and minima (Catuneanu et al., 2011; van Wagoner et al., 1988). For that reason, the L2/L3 boundary must predate the $\delta^{18}O$ maximum, and the maxima themselves must represent the eustatic low-stands of sea level, or LST of sequence stratigraphy, respectively. Thus, albeit seemingly counterintuitive, the sequence boundaries predating $\delta^{18}O$ maxima is consistent with theory and the $\delta^{18}O$ maxima to be considered equivalent with the LSTs (Figure 3).

A uniform duration of the elementary sequences associated with the long eccentricity cycle of 0.405 Myr is a likely scenario, in particular, as this cycle is present in many sedimentary records and the least influenced on the long-run by chaotic diffusion present in the Solar System than shorter periods around 0.1 Myr (Laskar et al., 2011). Eccentricity-dominated cyclicity has been described to occur preferentially in the shallowest segments of carbonate ramps systems of some Mesozoic Hothouse climates (Bádenas & Aurell, 2018), that we now identify as the primary pacemaker in our data of the shallow PB ramp (Figure 3 and Figure S3 in Supporting Information S1). Remarkably, most prominent of the long-term modulation of the 0.405 Myr component is the very long eccentricity related ∼2.4 Myr cycle that is a characteristic of the deep-sea record of the entire Cenozoic (Franceschi et al., 2015; Kocken et al., 2019; Laskar et al., 2011). We argue, therefore, that a global stratigraphic signature of PB paced by the 0.405 Myr eccentricity cycle should be complemented by a characteristic signa-ture of the ∼2.4 Myr cycle. For a verification, we use a comparative analysis of the long-term evolution of the shoreline trajectory and history of sedimentary accommodation space with the ∼2.4 Myr cycle expressed as the amplitude modulation of the long eccentricity cycle (Figure 3).

3.2.1. Variants of the Age Model and Their Relationship With the ~2.4 Myr Cycle

Here we present two separate age models to account for the two separate sequence stratigraphic variants pertaining to the nature of the L3/B1 boundary. In age model 1, we assume a continuous record (no hiatus) and elementary sequence #20 to represent the LST of B1, in model 2 elementary sequence #20 to represent the FSST of L3 and a hiatus to represent the LST of depositional sequence B1 (Figure 3). We assume a duration of one long eccentricity cycle for the hiatus which fits a previous estimate of the hiatus to span ~0.5 Ma (Gély & Lorenz, 1991; Pomerol, 1989). In both age models, we tune the mfs of the B1 sequence to the peak of the negative OIE of the MECO, while the duration of the single elementary sequences is kept constant at 0.405 Ma. Because of the hiatus in model 2, the age models differ by their basal ages of 48.8 and 49.2 Ma (Figure 3). Both calibrations are consistent with biostratigraphic tie-points, but age model 2 is qualitatively in better agreement with all available astronomical solutions (a, b, c, d) for the amplitude modulation of the eccentricity cycle and the long eccentricity cycle (Laskar et al., 2011) (Figure 3 and Figure S3 in Supporting Information S1). This latter model conforms best with the original hypothesis, that (a) the elementary sequences have an equal duration of 0.405 Myr, (b) the third order depositional sequences have heterogeneous durations, (c) no relevant hiatuses exist between both elementary sequences and sequences, respectively, and (d) a correlation with the astrochronologically dated global records of $\delta^{18}O$ (Westerhold et al., 2020) is feasible.

A certain exception in the correspondence between sequence architecture and eccentricity pattern is given by elementary sequences #1 to #4. While we take this bundle of elementary sequences as expression of the LST of the L1 sequence, they were originally described, quite consistent with the solution of the long eccentricity modulation, as a separate third-order sequence (Haq et al., 1987, 1988) (Figures 2 and 3, and Figure S3 in Supporting Information S1). However, based on the depositional geometries and facies evolution, these elementary sequences represent the LST of L1, while elementary sequence #5 represents the transgressive surface at the base of the subsequent TST (Figure 2). For that reason, we assume a sea-level cycle for these elementary sequences that is intermediate in magnitude between the third order and the elementary sequences.

Two further age models (models 3 and 4) were tied to the basal age of the BALCAT event of 49.2 Ma (Steurbaut & Nolf, 2021) and the lower boundaries of the lowest elementary sequences fine-tuned to a series of well-expressed short-term maxima of the 0.4 Myr-cycle in the orbitally calibrated global $\delta^{18}O$ record (Westerhold et al., 2020), leading to a basal age of 49.0 and 49.4 Ma, respectively (Figure S1 in Supporting Information S1).

3.3. Shoreline Trajectory

According to our age models, sequence L1 documents a long-term flooding phase of the basin (LST + TST) with a duration of ~4.0 Myr. Especially during the early flooding phase (LST), little sediment accumulation took place due to sediment starvation or condensation. In contrast to the flooding, the HST was comparatively short, lasting ~0.8 million years (Table 1, Figure 3). This broader long-term process can explain the spatially very extensive flooding of the basin by long-term subsidence of the basin despite of the long-term stillstand or even slow fall of eustatic sea level (Miller et al., 2020). Provided each of the elementary sequences is topped by an exposure surface, the stacking of shallowing upward cycles implies a successive, complete long-term filling of all available sediment accommodation space within the basin, while the shoreline trajectory of depositional sequence L1 documents some ~200 km of shoreline retreat over a period of 4.0 Myr, that is, ~50 km/Myr (Figure 3). Sequences L2 and L3 yield higher rates of shoreline retreat, ~100 km/0.8 Myr (125 km/Myr) and 100 km/0.4 Myr (250 km/Myr), respectively, but the reconstruction is less reliable than for L1 (methods) (Figure 3), and is therefore not part of the discussion below. In contrast to the L-sequences, the B1 sequence is formed of three elementary sequences only (Figure 3, Table 1). However, a total duration of 1.2 Ma of the B1 sequence exceeds the timeframe of the MECO, which is consistently reported to be between 0.4 and 0.6 Myr (Henehan et al., 2020; Rivero-Cuesta et al., 2019; Westerhold et al., 2020). This discrepancy results from the B1 sequence representing a full sea-level cycle with LST, TST and HST. In both age models elementary sequence #21 (Sables d'Auvers), reflecting extremely rapid flooding of the basin, is assigned to the TST, and elementary sequence #22, which partly includes terrestrial deposits (lacustrine limestone and eolian sand), is ascribed to the HST. Thus, maximum marine flooding (mfs) was reached between elementary sequences #21 and #22, after ~0.4 Ma. Because of the tuning of our age models, the mfs was equivalent with the peak of the MECO at ~40.3 Ma, while elementary sequence #22 postdates the peak of the MECO anomaly (Figure 3). This scenario also applies to age model 2, with the difference that we assume a hiatus of the duration of one long eccentricity

cycle between elementary sequences #20 and #21 (Gély & Lorenz, 1991; Pomerol, 1989) that we ascribe to a sea-level lowstand (Figure 3). Assuming that there was no coeval uplift or subsidence pulse during the early Bartonian in that part of the basin and mean subsidence did not deviate from the long-term middle Eocene trend (Guillocheau et al., 2000), sequence stratigraphic age model 2 is consistent with a pronounced sea-level lowstand prior to elementary sequence #21 during which the basin dried up. We consider this local lowstand equivalent with a pronounced global sea-level lowstand before the MECO inferred from the deep-sea record (Miller et al., 2020), and that we correlate with an astronomically calibrated $\delta^{18}O$ maximum ~41.0 Ma (Westerhold et al., 2020) (Figure 3). According to this calibration, a rapid flooding occurred with elementary sequence #21 when the coastline retreated by >200 km in a period of only 0.4 Myr (~500 km/Myr). At a rate of ~500 km/Myr, the retreat of the shoreline was ~10 times faster than during the flooding of the L1 sequence. However, this is only a minimum estimate for the flooding rate due to the limited resolution of our age model (0.4 Myr) and does not rule out even faster flooding.

3.4. Constraining Estimates of Middle Eocene Sea-Level Change

To constrain estimates of third order sea-level changes, we have used a Fischer Plot (Husinec et al., 2008; Sadler et al., 1993) and taken into account compaction (Figure 3 and Figure S4 in Supporting Information S1). Most obvious in the Fischer Plots is a long-term decrease of sediment accommodation space by ~20 m over sequences L1 through L3 and subsequent rapid rise of ~20 m during sequence B1 that displays a notable similarity to the long-term trend of global $\delta^{18}O$ (Westerhold et al., 2020) (Figure 3). However, the starting point and end point in a Fischer Plot being at 0 m represents an intrinsic characteristic of the method and the overall shape and slopes of the reconstruction strongly depend on the length of the time-window investigated (Sadler et al., 1993). The effect of the time-window length on the long-term shape of the plot is demonstrated in Figure 4 for age model 1 in Figures 4a and 4b and for age model 2 in Figures 4c and 4d. The presence of an inter-regional hiatus at the base of the Lutetian and a rather discontinuous record with common non-marine deposits during most of the Bartonian (Gély, 2016; Mégnien & Mégnien, 1980), that is, deposits being not accommodation limited by sea-level (e.g., eolian dunes) before the Sables des Cresnes (Gély & Lorenz, 1991), prevent modeling a time-window larger than the one presented here, however (Husinec et al., 2008; Sadler et al., 1993). The significance of the long-term 20 m decrease and short-term 20 m increase in accommodation space during the Lutetian and early Bartonian, respectively, is hard to assess, therefore, and depends on the kind of the subsequent B1 (Figure 4). Since these hypotheses cannot be evaluated using a Fischer plot, the long-term trend is not taken into account as necessarily real in our discussion below.

Unlike the long-term trend, the Fischer Plot allows reconstruction of third-order fluctuations of accommodation space that we equal with eustatic sea level variations (Figure 4). With respect to these fluctuations, an initial phase of negative deviation from mean cycle thickness followed by an increasingly positive deviation with a maximum in elementary sequence #8 can be read as reflecting a sea-level cycle with a ~15 m drop followed by a ~5 m rise and a renewed drop of ~8 m, consistent with the sequence stratigraphic inferences of an LST, TST, and HST (Figures 3 and 4). In this respect, the accommodation pattern of elementary sequences #1 to #4 is compatible with an interpretation as LST of the L1 sequence rather than a separate sequence (Haq et al., 1987, 1988) (Figures 2 and 3, Supporting Information S1). To obtain an estimate of the magnitude of the variations in accommodation space during cycles L2 and L3, we modeled the thicknesses of the individual elementary sequences, because individual thickness is not available for all elementary sequences in the published data sets (methods, Supporting Information S1). According to the modeling, we note variations in eustatic accommodation space of no more than 5–10 m for L2 and L3, compatible with the magnitude of change documented for L1 (Figures 3 and 4, Figure S3 in Supporting Information S1). It should be noted that the reconstruction for the third order sequences is independent from the long-term trend and time-window evaluated and remains in the order of 5–10 m (Figures 3 and 4). Similarly, independent from the choice of the time-window evaluated, the subsequent B1 sequence shows a rapid, short-term increase in accommodation space, which we quantify as ~20 m (Figure 2). This strong positive deviation from the mean thickness of the elementary sequences, coeval with the short-term flooding of the entire basin, implies a eustatic sea-level rise and maximum (Figure 3). In view of the fact that elementary sequences #21 and #22 document sediment underfilling and water depths of ≤10 m prior to their sudden subaerial exposure, a sea-level maximum of the order of ~30 m for the MECO is more likely. A uniform subsidence of the southern PB as we assume here for the Lutetian/Bartonian transition, has also been documented by long-term subsidence analyses (Guillocheau et al., 2000). Thus it is very unlikely that the rapid flooding of the basin during

the early Bartonian was due to a sudden subsidence pulse. Rather, uplift of the basin, as documented for its northern reaches during the latest Lutetian (Gély, 1996; Gély & Leroux, 2019) may have interfered negatively with an event of rapid creation of accommodation space by eustatic sea-level. Thus, because of simplifications related to sediment underfilling recognized for some of the elementary sequences, a hiatus by a eustatic lowstand (age model 2), and potential uplift, our current approach tends to underestimate true eustatic sea-level variation of B1 but gives a robust estimate of the overall magnitudes of sea-level change. For example, for elementary sequence #21, even when assuming a maximum water depth of ≤10 m, a ∼30 m sea-level rise would still be substantially less than ∼65 m inferred from the deep-sea record for the MECO (Miller et al., 2020), possibly also because we lack quantitative information on the lowstand of sea-level before that event in age model 2.

4. Significance of the Paris Basin Study

Our study provides an astronomically calibrated age model (age model 2) for the shallow-marine to terrestrial record of PB that is consistent with existing bio- and sequence stratigraphic knowledge (Figure 3 and Figure S2 in Supporting Information S1). The age model with a resolution of long eccentricity (0.405 Myr) is in accord with the concept that cyclic sequences of shallow marine carbonate platforms from the Hothouse worlds document accretionary dynamics paced by insolation driven cycles of sea level in the Milankovitch frequency band (Laskar et al., 2011; Read et al., 1995). Specifically, we observe correspondence between third order depositional sequences with the very long eccentricity cycle (2.4 Myr), factors which had been predicted earlier to be characteristically expressed in the shallow portions of carbonate platforms and ramps from the Hothouse geological periods (Bádenas & Aurell, 2018) and that we show now for the middle Eocene of PB.

4.1. Sea-Level Changes: Shoreline Trajectory and Fischer Plots

We use the shoreline trajectory for the definition and classification of depositional sequences. Third-order sea-level fluctuations in PB are represented by landward/seaward shifts of the shoreline in a horizontal distance of up to ≥200 km over the course of several million years (late Ypresian and Lutetian), or 0.405 Myr during the early Bartonian (MECO), respectively (Figure 3). Thus, long-term marine inundation of the basin associated with the MECO was at least one order of magnitude faster than during the Lutetian third order cycles (0.5 vs. 0.05 km/Kyr), but still extremely slow compared to the Pleistocene, post-glacial (12–6 ka) flooding of shallow basins, for example, the Persian Gulf with ∼130 km/Kyr (Lambeck, 1996). Lutetian eustatic sea-level amplitudes inferred from Fischer Plots were also startlingly small at <10 m. This value is significantly smaller than the 20–45 m of previous reconstructions of eustatic changes for the middle Eocene (de Graciansky et al., 1998; Miller et al., 2020; Pekar et al., 2003) that were derived indirectly from correlations to the global $\delta^{18}O$ curve by assuming a relationship with cryospheric dynamics (Pekar et al., 2003). In contrast, our conservative estimate is based directly on the lithological data of the sequences alone. The small amplitudes of the Lutetian third order cycles (L1–L3) found here were equivalent to a maximum change in the global $\delta^{18}O$ values of 0.10–0.13‰, when assuming an ice-effect *sensu* Pekar an co-workers (Pekar et al., 2003), but this potential ice-effect is so small for the Lutetian cycles as to be lost in data noise of the global $\delta^{18}O$ record (Figure 3).

With regard to the early Bartonian sea-level cycle of the MECO documented by sequence B1, our direct reconstruction of a ∼30 m of sea level rise is substantially higher than that for the Lutetian cycles. Although the siliciclastic sands of elementary sequence #21 underwent little compaction (Goldhammer, 1997) and the original water depth of ≤10 m can be accounted for on the basis of sedimentary structures and diverse biota, this is a minimum estimate, because of possible influences from subsurface uplift and an antecedent sea level lowstand that remains unquantified due to a hiatus. Nonetheless, a sea-level amplitude of ∼30 m is within the magnitude of glacioeustatic changes rather than thermally induced fluctuations (Miller et al., 2005), and an average rise of 30 m/0.4 Myr (0.075 m/Kyr) found by this study for the MECO is within the upper range of third order sea-level changes (0.01–0.1 m/ka) but still far below glacio-eustatic variability (Bentley et al., 2020; Miller et al., 2005). It should be noted, therefore, that our estimate being averaged over 0.4 Myr possibly integrates over a series of higher frequency cycles of the Milankovitch frequency band that are not resolved by our age model. Furthermore, maximum rates of sea level fall over the sequence boundaries L1/L2 and L2/L3 (SB2) were slower than the mean rate of subsidence of the basin, that is, slower than 0.011/0.010 m/Kyr (age model 1/2) which is at the lower endmember of third order sea-level changes (Bentley et al., 2020; Miller et al., 2005) and, therefore, very slow compared to high-frequency glacial dynamics as well.

With regard to the substantial difference in estimates of sea-level change by our study and those using $\delta^{18}O$ values from the deep-sea record (Miller et al., 2020; Pekar et al., 2003), it is possible that the temperature effect in the $\delta^{18}O$ data is underestimated and the glacioeustatic sea level fluctuation was in fact smaller than inferred in the global reconstructions (Henehan et al., 2020). Assuming sea-level rise documented by elementary sequence #21 records a glacioeustatic forcing (i.e., ice-volume effect on $\delta^{18}O$), and given a relationship of 0.10–0.13‰ per 10 m of sea-level change (Pekar et al., 2003), the global negative OIE of the MECO of ∼1.0‰ would have a minimum of 0.3‰ glacioeustatic component, and correspondingly global temperature increase inferred from $\delta^{18}O$ data would be ≤3°C (assuming a $\delta^{18}O$ change of −0.23‰ per °C (Böhm et al., 2000)): much smaller than originally inferred (Bohaty et al., 2009; Bohaty & Zachos, 2003). While this would appear at odds with TEX_{86}^{H} records that suggest a ∼3°C rise in the tropics (Cramwinckel et al., 2018) and up to ∼6°C in high latitudes (Cramwinckel et al., 2018), it would be consistent with TEX_{86}^{H} records that show a much more muted 2°C change in temperature (Cramwinckel et al., 2020), or no change at all (van der Ploeg et al., 2023).

4.2. Implications for Middle Eocene Sea Level Changes: Orbital Configuration, Greenhouse Gas Forcing and Glacioeustasy

The age model of the mid-Eocene PB sea-level record implies a profound synchronicity of the long-term sea-level record with the amplitude modulation of the long eccentricity cycle. Except for the MECO, minima and maxima of the very long eccentricity amplitude modulation of eccentricity coincide with minima and maxima in eustatic sea level (third order) of our reconstruction (Figure 3 and Figure S3 in Supporting Information S1). Roughly 400 Kyr long intervals of low eccentricity amplitude modulations, often referred to as nodes, occur at 40.25, 43.1, 45.1, and 48 Ma using La2011b or La2011c solutions which show the best match to geological data (Westerhold et al., 2017) in the early to middle Eocene. The PB record, with exception at 40.25 Ma where the MECO occurred, shows sequence boundaries indicating third order sea level lowstands. During the nodes in the eccentricity cycle, when the amplitude modulation of precession by eccentricity is low, obliquity related cyclicity is more likely to be apparent in climate records. For late Eocene deep sea records this was observed during nodes around 35.5, 38.3, and 40.1 Ma (Westerhold et al., 2014) and the early to middle Eocene around 50 Ma (Westerhold & Röhl, 2013). During nodes of eccentricity the seasonal climate can be expected to be more uniform as insolation variations will be dampened by low eccentricity modulations of precession. Vice versa, higher eccentricity amplitude modulations of precession will promote larger amplitude insolation fluctuation. Thus, during the duration of a 2.4 Myr eccentricity node higher insolation values are absent and will facilitate accumulation of polar ice. Because temperature related fluctuation in sea level will also be rather insignificant during the nodes, polar ice mass could affect sea level globally. Here we hypothesize that during or toward the 2.4 Myr eccentricity nodes at 43.1, 45.1, and 48 Ma, polar ice mass growth drove the observed third order sea level fluctuations in the PB, consistent with recent models for the Late Eocene (Van Breedam et al., 2022). The presence of marine-terminating glaciers sensitive to climatic perturbations and of "substantial volume" existed in the East Antarctic already by the early to middle Eocene (Gulick et al., 2017), and occurrence of ice and ice-rafted debris has been reported for the Arctic around 47–46 Ma (St. John, 2008; Stickley et al., 2009) and ∼44–45 Ma (GTS2012) already (Cramwinckel et al., 2018), supporting this assertion. Conversely, times of higher amplitude eccentricity modulation of insolation polar ice could have been diminished again, raising sea level.

For the MECO event, the pattern of high sea level/maximum eccentricity cycle amplitude (minimum amplitude of the long eccentricity cycle) is apparently reversed by the coincidence of a sea level maximum with a minimum eccentricity amplitude (minimum of the long eccentricity cycle amplitude modulation) (Figure 3 and Figure S3 in Supporting Information S1). As such it seems to deviate from the common patterns of warm climates being favored by high-eccentricity configurations (Vahlenkamp et al., 2020; Westerhold & Röhl, 2013; Zeebe et al., 2017) and argue for a mechanism independent of astronomical forcings, such as a rise of atmospheric CO_2 from paroxysmal volcanic eruptions or other sources (Cramwinckel et al., 2018; Henehan et al., 2020; van der Boon et al., 2021). Thus, the alleged misfit of the age model presented with the 2.4 Myr astronomical pattern is compatible with a telluric climatic forcing dominating the climate system of the MECO in the short term and overriding the effect of the astronomically controlled insolation changes. Given a drop in surface ocean pH of ∼0.2 during the MECO (Henehan et al., 2020), the spectacular skeletal preservation of many PB fossils (Brachert et al., 2022; Merle, 2008) may therefore allow us to examine the impact on epicontinental shelf ecosystems. In particular, currently it is unclear whether the MECO surface ocean was buffered at constant carbonate saturation state by silicate weathering (Henehan et al., 2020), or whether a reduced weathering feedback (Krause et al., 2023;

van der Ploeg et al., 2018) meant that this drop in ocean pH also coincided with a drop in ocean carbonate saturation, and thereby "true" ocean acidification (Hönisch et al., 2012). Future studies of calcification patterns in the PB over the MECO could therefore inform as to the dynamics of the silicate weathering feedback over this enigmatic event, and in doing so help to constrain atmospheric CO_2 levels at this time (Henehan et al., 2020).

Conflict of Interest

The authors declare no conflicts of interest relevant to this study.

Data Availability Statement

All data underlying this research have been published or are given in Table 1 of the manuscript (Abrard, 1925; Aubry, 1983, 1985; Blondeau, 1965; Briais, 2015; Cavelier & Le Calvez, 1965; Chateauneuf & Gruas-Cavagnetto, 1978; Gély, 1996; Gély & Leroux, 2019; Mégnien & Mégnien, 1980; Merle, 2008; Steurbaut & Nolf, 2021). Table 1 is available at Zenodo (Brachert et al., 2023).

Acknowledgments
Antun Husinec is thanked for providing a preformatted excel spreadsheet for Fischer Plots and fruitful discussions. Funding by the Deutsche Forschungsgemeinschaft (DFG, German Research Foundation)—Project number 468644633 (T.C.B.)—SPP 2299/Project number 441832482 "Tropical climate variability & coral reefs" is gratefully acknowledged. Thomas Westerhold was funded by the Deutsche Forschungsgemeinschaft (DFG, German Research Foundation) under Germany's Excellence Strategy—EXC-2077—390741603. Open Access funding enabled and organized by Projekt DEAL.

References

Abrard, R. (1925). *Le Lutétien du bassin de Paris: Essai de monographie stratigraphique* (p. 383). Société française d'imprimerie d'Angers.
Agnini, C., Fornaciari, E., Raffi, I., Catanzariti, R., Pälike, H., Backman, J., & Rio, D. (2014). Biozonation and biochronology of Paleogene calcareous nannofossils from low and middle latitudes. *Newsletter on Stratigraphy*, *47*(2), 131–181. https://doi.org/10.1127/0078-0421/2014/0042
Aubry, M.-P. (1983). Biostratigraphie du paleogene epicontinental de!'Europe du Nord-Ouest, etude fondee sur les nannofossiles calcaires. *Documents des Laboratories de Geologie de Lyon*, *89*, 317.
Aubry, M.-P. (1985). Northwestern European Paleogene magnetostratigraphy, biostratigraphy, and paleogeography: Calcareous nannofossil evidence. *Geology*, *13*(3), 198–202. https://doi.org/10.1130/0091-7613(1985)13<198:nepmba>2.0.co;2
Bádenas, B., & Aurell, M. (2018). The down-dip preferential sequence record of orbital cycles in greenhouse carbonate ramps: Examples from the Jurassic of the Iberian Basin (NE Spain). In M. Montenari (Ed.), *Stratigraphy & timescales* (pp. 285–325). Academic Press.
Barrier, E., Vrielynck, B., Brouillet, J.-F., & Brunet, M.-F. (2018). Paleotectonic reconstruction of the Central Tethyan Realm. Tectono-sedimentary-Palinspastic maps from Late Permian to Pliocene. 20 maps.
Bentley, C., Layou, K., Kohrs, R., Jaye, S., Affolter, M., & Ricketts, B. (2020). *Historical geology*. A free online text "book". WordPress.
Blondeau, A. (1965). Le Lutétien des Bassin de Paris, de Belgique et du Hampshire (Dissertation thesis) (p. 467). University of Paris.
Bohaty, S. M., & Zachos, J. C. (2003). Significant Southern Ocean warming event in the late middle Eocene. *Geology*, *31*(11), 1017–1020. https://doi.org/10.1130/g19800.1
Bohaty, S. M., Zachos, J. C., Florindo, F., & Delaney, M. L. (2009). Coupled greenhouse warming and deep-sea acidification in the Middel Eocene. *Paleoceanography*, *24*(2), PA2207. https://doi.org/10.1029/2008pa001676
Böhm, F., Joachimski, M. M., Dullo, W.-C., Eisenhauer, A., Lehnert, H., Reitner, J., & Wörheide, G. (2000). Oxygen isotope fractionation in marine aragonite of coralline sponges. *Geochimica et Cosmochimica Acta*, *64*(10), 1695–1703. https://doi.org/10.1016/s0016-7037(99)00408-1
Brachert, T. C., Agnini, C., Gagnaison, C., Gély, J.-P., Henehan, M. J., & Westerhold, T. (2023). Astronomical pacing of middle Eocene sea-level fluctuations: Inferences from shallow-water carbonate ramp deposits [Dataset]. Paleoceanography and Paleoclimatology. Zenodo. https://doi.org/10.5281/zenodo.8305712
Brachert, T. C., Felis, T., Gagnaison, C., Hoehle, M., Reuter, M., & Spreter, P. M. (2022). Slow-growing reef corals as climate archives: A case study of the Middle Eocene Climatic Optimum 40 Ma ago. *Science Advances*, *8*(20), eabm3875. https://doi.org/10.1126/sciadv.abm3875
Briais, J. (2015). Le Cénozoïque du bassin de Paris: Un enregistrement sédimentaire haute résolution des déformations lithosphériques en régime de faible subsidence (Dissertation thesis) (p. 451). Rennes University.
Briais, J., Guillocheau, F., Lasseur, E., Robin, C., Châteauneuf, J. J., & Serrano, O. (2016). Response of a low-subsiding intracratonic basin to long wavelength deformations: The Palaeocene-early Eocene period in the Paris Basin. *Solid Earth*, *7*(1), 205–228. https://doi.org/10.5194/se-7-205-2016
Brigaud, B., Bonifacie, M., Pagel, M., Blaise, T., Calmels, D., Haurine, F., & Landrein, P. (2020). Past hot fluid flows in limestones detected by Δ47–(U-Pb) and not recorded by other geothermometers. *Geology*, *48*(9), 851–856. https://doi.org/10.1130/g47358.1
Catuneanu, O., Galloway, W. E., Kendall, C. G. S. E., Miall, A. D., Posamentier, H. W., Strasser, A., & Tucker, M. E. (2011). Sequence stratigraphy: Methodology and nomenclature. *Newsletters on Stratigraphy*, *44*(3), 173–245. https://doi.org/10.1127/0078-0421/2011/0011
Cavelier, C., & Le Calvez, Y. (1965). Présence d'*Arenagula kerfornei* (Allix), foraminifère 'biarritzien', à la partie terminale du Lutétien supérieur de Foulangues (Oise). *Bulletin de la Société Géologique de France*, *S7-VII*(2), 284–286. https://doi.org/10.2113/gssgfbull.s7-vii.2.284
Chateauneuf, J.-J., & Gruas-Cavagnetto, C. (1978). Les zones des Wetzeliellaceae (Dinophyceae) du bassin de Paris. *Bulletin du B.R.G.M. (deuxième série)*, *2-1978*, 59–93.
Cramer, B. S., Miller, K. G., Barrett, P. J., & Wright, J. D. (2011). Late Cretaceous-Neogene trends in deep ocean temperature and continental ice volume: Reconciling records of benthic foraminiferal geochemistry ($\delta^{18}O$ and Mg/Ca) with sea level history. *Journal of Geophysical Research*, *116*(C12), C12023. https://doi.org/10.1029/2011jc007255
Cramwinckel, M. J., Coxall, H. K., Śliwińska, K. K., Polling, M., Harper, D. T., Bijl, P. K., et al. (2020). A warm, stratified, and restricted Labrador Sea across the Middle Eocene and its climatic optimum. *Paleoceanography and Paleoclimatology*, *35*(10), e2020PA003932. https://doi.org/10.1029/2020pa003932
Cramwinckel, M. J., Huber, M., Kocken, I. J., Agnini, C., Bijl, P. K., Bohaty, S. M., et al. (2018). Synchronous tropical and polar temperature evolution in the Eocene. *Nature*, *559*(7714), 382–386. https://doi.org/10.1038/s41586-018-0272-2
Dawber, C. F., Tripati, A. K., Gale, A. S., MacNiocaill, C., & Hesselbo, S. P. (2011). Glacioeustasy during the middle Eocene? Insights from the stratigraphy of the Hampshire Basin, UK. *Palaeogeography, Palaeoclimatology, Palaeoecology*, *300*(1), 84–100. https://doi.org/10.1016/j.palaeo.2010.12.012

de Graciansky, P.-C., Hardenbol, J., Jacquin, T., & Vail, P. R. (1998). Mesozoic and Cenozoic sequence stratigraphy of European basins.
Edgar, K. M., Bohaty, S. M., Coxall, H. K., Bown, P. R., Batenburg, S. J., Lear, C. H., & Pearson, P. N. (2020). New composite bio- and isotope stratigraphies spanning the Middle Eocene Climatic Optimum at tropical ODP Site 865 in the Pacific Ocean. *Journal of Micropalaeontology*, *39*(2), 117–138. https://doi.org/10.5194/jm-39-117-2020
Edgar, K. M., Wilson, P. A., Sexton, P. F., & Suganuma, Y. (2007). No extreme bipolar glaciation during the main Eocene calcite compensation shift. *Nature*, *448*(7156), 908–911. https://doi.org/10.1038/nature06053
Fischer, A. G. (1964). The Lofer cyclothems of the Alpine Triassic. In D. F. Merriam (Ed.), *Symposium on cyclic sedimentation*, *Kansas Geological Survey Bulletin* (Vol. 169, pp. 107–149).
Fornaciari, E., Agnini, C., Catanzariti, R., Rio, D., Bolla, E. M., & Valvasoni, E. (2010). Mid-latitude calcareous nannofossil biostratigraphy and biochronology across the middle to late Eocene transition. *Stratigraphy*, *7*(4), 229–264.
Franceschi, M., Penasa, L., Coccioni, R., Gattacceca, J., Smit, J., Cascella, A., et al. (2015). Terrestrial Laser Scanner imaging for the cyclostratigraphy and astronomical tuning of the Ypresian–Lutetian pelagic section of Smirra (Umbria–Marche Basin, Italy). *Palaeogeography, Palaeoclimatology, Palaeoecology*, *440*, 36–46. https://doi.org/10.1016/j.palaeo.2015.08.027
Gall, J.-C. (1983). *Sedimentationsräume und Lebensbereiche der Erdgeschichte - Eine Einführung in die Paläoökologie*. Springer-Verlag.
Gély, J.-P. (1996). Le Lutétien du Bassin Parisien: De l'analyse séquentielle haute résolution à la reconstitution paléogéographique. *Bulletin d'Information des Géologues du Bassin de Paris*, *34*(2), 3–27.
Gély, J.-P. (2016). Le Paléogène du Bassin du Paris: Corrélations et reconstitutions paléogéographiques. *Bulletin d'Information des Géologues du Bassin de Paris*, *53*(4), 2–13.
Gély, J.-P., & Leroux, L. (2019). Les pierres d'appareil du Lutétien du bassin de Paris: Une ressource complexe et diverse. *Bulletin d'Information des Géologues du Bassin de Paris*, *56*(4), 26–39.
Gély, J. P., & Lorenz, C. (1991). Analyse séquentielle de l'Eocène et de l'Oligocène du bassin Parisien (France). *Revue Institut Francais de Pétrole*, *46*(6), 713–747. https://doi.org/10.2516/ogst:1991034
Giorgioni, M., Jovane, L., Rego, E. S., Rodelli, D., Frontalini, F., Coccioni, R., et al. (2019). Carbon cycle instability and orbital forcing during the Middle Eocene Climatic Optimum. *Scientific Reports*, *9*(1), 9357. https://doi.org/10.1038/s41598-019-45763-2
Goldhammer, R. (1997). Compaction and decompaction algorithms for sedimentary carbonates. *Journal of Sedimentary Research*, *67*, 26–35. https://doi.org/10.1306/d42684e1-2b26-11d7-8648000102c1865d
Gradstein, F. M., Ogg, J. G., Schmitz, M. D., & Ogg, G. M. (2020). *Geologic time scale 2020*. Elsevier.
Guillocheau, F., Robin, C., Allemand, P., Bourquin, S., Brault, N., Dromart, G., et al. (2000). Meso-Cenozoic geodynamic evolution of the Paris Basin: 3D stratigraphic constraints. *Geodinamica Acta*, *13*(4), 189–246. https://doi.org/10.1080/09853111.2000.11105372
Gulick, S. P. S., Shevenell, A. E., Montelli, A., Fernandez, R., Smith, C., Warny, S., et al. (2017). Initiation and long-term instability of the East Antarctic Ice Sheet. *Nature*, *552*(7684), 225–229. https://doi.org/10.1038/nature25026
Haq, B. U., Hardenbol, J., & Vail, P. R. (1987). Chronology of fluctuating sea levels since the Triassic. *Science*, *235*(4793), 1156–1167. https://doi.org/10.1126/science.235.4793.1156
Haq, B. U., Hardenbol, J., & Vail, P. R. (1988). Mesozoic and Cenozoic chronostratigraphy and eustatic cycles. In C. K. Wilgus, B. S. Hastings, C. G. S. C. Kendall, H. W. Posamentier, C. A. Ross, & J. C. Van Wagoner (Eds.), *Sea-level changes: An integrated approach* (pp. 71–108). SEPM Special Publication No. 42.
Hardenbol, J., Thierry, J., Farley, M. B., Jacquin, T., de Graciansky, P.-C., & Vail, P. R. (1998). Mesozoic and Cenozoic sequence stratigraphic framework of European Basins. In P.-C. de Graciansky, J. Hardenbol, J. Thierry, & P. R. Vail (Eds.), *Mesozoic and Cenozoic sequence stratigraphy of European Basins* (pp. 3–13). Society for Sedimentary Geology.
Hardie, L. A., & Shinn, E. A. (1986). Carbonate depositional environments, modern and ancient. Part 3 - Tidal flats. *Colorado School of Mines Quarterly*, *81*(1), 1–74.
Henehan, M. J., Edgar, K. M., Foster, G. L., Penman, D. E., Hull, P. M., Greenop, R., et al. (2020). Revisiting the Middle Eocene climatic optimum "Carbon Cycle Conundrum" with new estimates of atmospheric pCO_2 from boron isotopes. *Paleoceanography and Paleoclimatology*, *35*(6), e2019PA003713. https://doi.org/10.1029/2019pa003713
Hönisch, B., Ridgwell, A., Schmidt, D. N., Thomas, E., Gibbs, S. J., Sluijs, A., et al. (2012). The geological record of ocean acidification. *Science*, *335*(6072), 1058–1063. https://doi.org/10.1126/science.1208277
Husinec, A., Basch, D., Rosec, B., & Read, J. F. (2008). FISCHERPLOTS: An Excel spreadsheet for computing Fischer plots of accommodation change in cyclic carbonate successions in both the time and depth domains. *Computers & Geosciences*, *34*(3), 269–277. https://doi.org/10.1016/j.cageo.2007.02.004
Kocken, I. J., Cramwinckel, M. J., Zeebe, R. E., Middelburg, J. J., & Sluijs, A. (2019). The 405 kyr and 2.4 Myr eccentricity components in Cenozoic carbon isotope records. *Climate of the Past*, *15*(1), 91–104. https://doi.org/10.5194/cp-15-91-2019
Kominz, M. A., Browning, J. V., Miller, K. G., Sugarman, P. J., Mizintseva, S., & Scotese, C. R. (2008). Late Cretaceous to Miocene sea-level estimates from the New Jersey and Delaware coastal plain corehole: An error analysis. *Basin Research*, *20*, 221–226.
Krause, A. J., Sluijs, A., van der Ploeg, R., Lenton, T. M., & Pogge von Strandmann, P. A. E. (2023). Enhanced clay formation key in sustaining the Middle Eocene Climatic Optimum. *Nature Geoscience*, *16*(8), 730–738. https://doi.org/10.1038/s41561-023-01234-y
Lambeck, K. (1996). Shoreline reconstructions for the Persian Gulf since the last glacial maximum. *Earth and Planetary Science Letters*, *142*(1), 43–57. https://doi.org/10.1016/0012-821x(96)00069-6
Laskar, J., Fienga, A., Gastineau, M., & Manche, H. (2011). La2010: A new orbital solution for the long-term motion of the Earth. *Astronomy and Astrophysics*, *A89*, 15.
Martini, E. (1971). Standard Tertiary and Quaternary calcareous nannoplankton zonation. In *Paper presented at proceedings of the II planktonic conference, Roma*. Tecnoscienza.
Martín-Martín, M., Guerrera, F., Tosquella, J., & Tramontana, M. (2021). Middle Eocene carbonate platforms of the westernmost Tethys. *Sedimentary Geology*, *415*, 1–25. https://doi.org/10.1016/j.sedgeo.2021.105861
Mégnien, C., & Mégnien, F. (1980). *Synthèse géologique du bassin de Paris. Volume 1. Stratigraphie et paléogéographie* (p. 46). B.R.G.M.
Merle, D. (Ed.). (2008). *Stratotype lutétien* (p. 288). Muséum National d'Histoire Naturelle, Biotope, BRGM.
Miller, K. G., Browning, J. V., Schmelz, W. J., Kopp, R. E., Mountain, G. S., & Wright, J. D. (2020). Cenozoic sea-level and cryospheric evolution from deep-sea geochemical and continental margin records. *Science Advances*, *6*(20), eaaz1346. https://doi.org/10.1126/sciadv.aaz1346
Miller, K. G., Kominz, M. A., Browning, J. V., Wright, J. D., Mountain, G. S., Katz, M. E., et al. (2005). The Phanerozoic record of global sea-level change. *Science*, *310*(5752), 1293–1298. https://doi.org/10.1126/science.1116412
Molina, E., Alegret, L., Apellaniz, E., Bernaola, G., Caballero, F., Dinarès-Turell, J., et al. (2011). The Global Stratotype Section and Point (GSSP) for the base of the Lutetian Stage at the Gorrondatxe section, Spain. *Episodes*, *34*(2), 86–107. https://doi.org/10.18814/epiiugs/2011/v34i2/006

Pekar, S. F., Hucks, A., Fuller, M., & Li, S. (2003). Glacioeustatic changes in the early and middle Eocene (51–42 Ma): Shallow-water stratigraphy from ODP Leg 189 Site 1171 (South Tasman Rise) and deep-sea δ18O recods. *Geological Society of America Bulletin*, *117*(7), 1081–1093. https://doi.org/10.1130/b25486.1

Peters, S. E., Carlson, A. E., Kelly, D. C., & Gingerich, P. D. (2010). Large-scale glaciation and deglaciation of Antarctica during the Late Eocene. *Geology*, *38*(8), 723–726. https://doi.org/10.1130/g31068.1

Pomerol, C. (1981). Stratotypes of Paleogene stages (p. 301).

Pomerol, C. (1989). Stratigraphy of the Palaeogene: Hiatuses and transitions. *Proceedings of the Geological Association*, *100*(3), 313–324. https://doi.org/10.1016/s0016-7878(89)80051-3

Read, J. F., Kerans, C., Weber, L. J., Sarg, J. F., & Wright, F. M. (1995). Milankovitch sea-level changes, cycles, and reservoirs on carbonate platforms in Greenhouse and Ice-house worlds. *Society of Economic Palaeontologists and Mineralogists, Short course*, *35*, 1–81.

Rivero-Cuesta, L., Westerhold, T., Agnini, C., Dallanave, E., Wilkens, R. H., & Alegret, L. (2019). Paleoenvironmental changes at ODP Site 702 (South Atlantic): Anatomy of the Middle Eocene climatic optimum. *Paleoceanography and Paleoclimatology*, *34*(12), 2047–2066. https://doi.org/10.1029/2019pa003806

Sadler, P. M., Osleger, D. A., & Montañez, I. P. (1993). On the labeling, length and objective basis of Fischer plots. *Journal of Sedimentary Petrology*, *63*, 360–368. https://doi.org/10.1306/d4267aff-2b26-11d7-8648000102c1865d

Schlager, W. (1992). Sedimentology and sequence stratigraphy of reefs and carbonate platforms, a short course. *The American Association of Petroleum Geologists, Continuing Education Course Note Series*, *34*, 1–71.

Scholle, P. A., Bebout, D. G., & Moore, C. H. (Eds.). (1983). *Carbonate depositional environments* (p. 708). American Association of Petroleum Geologists Memoir 33.

Shi, J., Jin, Z., Liu, Q., Zhang, R., & Huang, Z. (2019). Cyclostratigraphy and astronomical tuning of the middle Eocene terrestrial successions in the Bohai Bay Basin, Eastern China. *Global and Planetary Change*, *174*, 115–126. https://doi.org/10.1016/j.gloplacha.2019.01.001

Sluijs, A., Zeebe, R. E., Bijl, P. K., & Bohaty, S. M. (2013). A middle Eocene carbon cycle conundrum. *Nature Geoscience*, *6*(6), 429–434. https://doi.org/10.1038/ngeo1807

Steurbaut, E., & Nolf, D. (2021). The Mont-des-Récollets section (N France): A key site for the Ypresian-Lutetian transition at mid-latitudes – Reassessment of the boundary criterion for the base-Lutetian GSSP. *Geodiversitas*, *43*(11), 311–363. https://doi.org/10.5252/geodiversitas2021v43a11

Stickley, C. E., St John, K., Koç, N., Jordan, R. W., Passchier, S., Pearce, R. B., & Kearns, L. E. (2009). Evidence for middle Eocene Arctic sea ice from diatoms and ice-rafted debris. *Nature*, *460*(7253), 376–379. https://doi.org/10.1038/nature08163

St. John, K. (2008). Cenozoic ice-rafting history of the central Arctic Ocean: Terrigenous sands on the Lomonosov Ridge. *Paleoceanography*, *23*(1), PA1S05. https://doi.org/10.1029/2007pa001483

Strasser, A. (2018). Cyclostratigraphy of shallow-marine carbonates - Limitations and opportunities. *Stratigraphy and Timescales*, *3*, 151–187.

Tripati, A. K., Backman, J., Elderfield, H., & Ferretti, P. (2005). Eocene bipolar glaciation associated with global carbon cycle changes. *Nature*, *436*(7049), 341–346. https://doi.org/10.1038/nature03874

Vahlenkamp, M., De Vleeschouwer, D., Batenburg, S. J., Edgar, K. M., Hanson, E., Martinez, M., et al. (2020). A lower to middle Eocene astrochronology for the Mentelle Basin (Australia) and its implications for the geologic time scale. *Earth and Planetary Science Letters*, *529*, 115865. https://doi.org/10.1016/j.epsl.2019.115865

Vail, P. R., & Mitchum, R. M., Jr. (1977). Seismic stratigraphy and global changes of sea level, Part one: Overview. In C. E. Payton (Ed.), *Seismic stratigraphy—Applications to hydrocarbon exploration* (pp. 51–52). American Association of Petroleum Geologists Memoir 26.

Vail, P. R., Mitchum, R. M., Jr., Todd, R. G., Widmier, J. M., Thompson, S., III, Sangree, J. B., et al. (1977). *Seismic stratigraphy and global changes of sea level* (pp. 49–212). American Association of Petroleum Geologists Memoir, 26.

Van Breedam, J., Huybrechts, P., & Crucifix, M. (2022). Modelling evidence for late Eocene Antarctic glaciations. *Earth and Planetary Science Letters*, *586*, 117532. https://doi.org/10.1016/j.epsl.2022.117532

van der Boon, A., Kuiper, K. F., van der Ploeg, R., Cramwinckel, M. J., Honarmand, M., Sluijs, A., & Krijgsman, W. (2021). Exploring a link between the Middle Eocene Climatic Optimum and Neotethys continental arc flare-up. *Climate of the Past*, *17*(1), 229–239. https://doi.org/10.5194/cp-17-229-2021

van der Ploeg, R., Cramwinckel, M. J., Kocken, I. J., Leutert, T. J., Bohaty, S. M., Fokkema, C. D., et al. (2023). North Atlantic surface ocean warming and salinization in response to middle Eocene greenhouse warming. *Science Advances*, *9*(4), eabq0110. https://doi.org/10.1126/sciadv.abq0110

van der Ploeg, R., Selby, D., Cramwinckel, M. J., Li, Y., Bohaty, S. M., Middelburg, J. J., & Sluijs, A. (2018). Middle Eocene greenhouse warming facilitated by diminished weathering feedback. *Nature Communications*, *9*(1), 2877. https://doi.org/10.1038/s41467-018-05104-9

van Hinsbergen, D. J. J., de Groot, L. V., van Schaik, S. J., Spakman, W., Bijl, P. K., Sluijs, A., et al. (2015). A Paleolatitude calculator for Paleoclimate studies (model version 2.1). *PLoS One*, *10*(6), e0126946. https://doi.org/10.1371/journal.pone.0126946

van Hinte, J. E. (1978). Geohistory analysis—Application of micropaleontology in exploration geology. *American Association of Petroleum Geologists Bulletin*, *62*, 201–222. https://doi.org/10.1306/c1ea4815-16c9-11d7-8645000102c1865d

van Wagoner, J. C., Posamentier, H. W., Mitchum, R. M., Vail, P. R., Sarg, J. F., Loutit, T. S., & Hardenbol, J. (1988). An overview of the fundamentals of sequence stratigraphy and key defiitions. In *Sea-level changes - An integrated approach* (pp. 39–45).

Villa, G., Florindo, F., Persico, D., Lurcock, P., de Martini, A. P., Jovane, L., & Fioroni, C. (2021). Integrated calcareous nannofossil and magnetostratigraphic record of ODP Site 709: Middle Eocene to late Oligocene paleoclimate and paleoceanography of the Equatorial Indian Ocean. *Marine Micropaleontology*, *169*, 102051. https://doi.org/10.1016/j.marmicro.2021.102051

Wallace, C. C., & Rosen, B. R. (2006). Diverse staghorn corals (*Acropora*) in high-latitude Eocene assemblages: Implications for the evolution of modern diversity patterns of reef corals. *Proceedings of the Royal Society B: Biological Sciences*, *273*(1589), 975–982. https://doi.org/10.1098/rspb.2005.3307

Westerhold, T., Marwan, N., Drury, A. J., Liebrand, D., Agnini, C., Anagnostou, E., et al. (2020). An astronomically dated record of Earth's climate and its predictability over the last 66 million years. *Science*, *369*(6509), 1383–1387. https://doi.org/10.1126/science.aba6853

Westerhold, T., & Röhl, U. (2013). Orbital pacing of Eocene climate during the Middle Eocene Climate Optimum and the chron C19r event: Missing link found in the tropical western Atlantic. *Geochemistry, Geophysics, Geosystems*, *14*(11), 4811–4825. https://doi.org/10.1002/ggge.20293

Westerhold, T., Röhl, U., Donner, B., Frederichs, T., Kordesch, W., Bohaty, S., et al. (2017). Late Lutetian Thermal Maximum: Crossing a Thermal Threshold in Earth's Climate System? *Geochemistry, Geophysics, Geosystems*, *19*(1), 73–82. https://doi.org/10.1002/2017gc007240

Westerhold, T., Röhl, U., Pälike, H., Wilkens, R., Wilson, P. A., & Acton, G. (2014). Orbitally tuned timescale and astronomical forcing in the middle Eocene to early Oligocene. *Climate of the Past*, *10*(3), 955–973. https://doi.org/10.5194/cp-10-955-2014

Westerhold, T., Röhl, U., Wilkens, R. H., Gingerich, P. D., Clyde, W. C., Wing, S. L., et al. (2018). Synchronizing early Eocene deep-sea and continental records – Cyclostratigraphic age models for the Bighorn Basin Coring Project drill cores. *Climate of the Past*, *14*(3), 303–319. https://doi.org/10.5194/cp-14-303-2018

White, C. H. (2013). Corals and climate change in the Cenozoic; A case study based on the staghorn coral *Acropora* (Dissertation thesis) (p. 476). University of London.

Zeebe, R. E., Westerhold, T., Littler, K., & Zachos, J. C. (2017). Orbital forcing of the Paleocene and Eocene carbon cycle. *Paleoceanography*, *32*(5), 440–465. https://doi.org/10.1002/2016pa003054

References From the Supporting Information

Aubry, M.-P. (1986). Paleogene calcareous nannoplankton biostratigraphy of northwestern Europe. *Palaeogeography, Palaeoclimatology, Palaeoecology*, *55*(2–4), 267–334. https://doi.org/10.1016/0031-0182(86)90154-9

Huyghe, D., Lartaud, F., Emmanuel, L., Merle, D., & Renard, M. (2015). Paleogene climate evolution in the Paris Basin from oxygen stable isotope ($\delta^{18}O$) compositions of marine molluscs. *Journal of the Geological Society*, *172*, 1–12.

Miall, A. D. (1997). *The geology of stratigraphic sequences* (1 ed., p. 433). Springer.